# Heterogeneous but not random: Cargo degradation in phagosomes is kinetically coupled to their intracellular mobility

Yanqi Yu[1]†, Zihan Zhang[1]†, Glenn F. W. Walpole[2,3], and Yan Yu[1]*

[1]Department of Chemistry, Indiana University, Bloomington, IN 47405-7102

[2]Program in Cell Biology, The Hospital for Sick Children, Toronto, Ontario, Canada

[3]Department of Biochemistry, University of Toronto, Ontario, Canada

† Y.-q. Y. and Z. Z. contributed equally to this work

*Corresponding Author: Yan Yu, Department of Chemistry, Indiana University, Bloomington, IN 47405-7102, phone 812-855-0593 Email, yy33@iu.edu

## Abstract

Immune cells degrade internalized pathogens in phagosomes through sequential biochemical changes. The degradation must be fast enough for effective infection control. The presumption is that each phagosome degrades cargos autonomously with a distinct but stochastic kinetic rate. Here we report that the degradation kinetics of individual phagosomes is not stochastic but coupled to their intracellular motility. By engineering RotSensors that are optically anisotropic, magnetic responsive, and fluorogenic in response to degradation activities in phagosomes, we monitored cargo degradation kinetics in single phagosomes simultaneously with their translational and rotational dynamics. We show that phagosomes that move faster centripetally are more likely to encounter and fuse with lysosomes, thereby acidifying faster and degrading cargos more efficiently. The degradation rates increase nearly linearly with the translational and rotational velocities of

26 phagosomes. Our results indicate that the centripetal motion of phagosomes functions as a clock
27 for controlling the progression of cargo degradation.
28

29 **Introduction**

30 Innate immune cells, such as macrophages, ingest pathogens and dead cells via a phagocytosis
31 process. This is an essential process in infection control and tissue homeostasis. After recognizing
32 ligands on pathogens, immune cells internalize them into phagosomes and transport them from the
33 cell periphery to the perinuclear region[1, 2, 3, 4, 5]. During this intracellular transport, phagosomes
34 degrade the entrapped pathogens through sequential biochemical transformations, including the
35 acidification of the lumen[6], the activation of hydrolytic enzymes[7], and the generation of reactive
36 oxygen species (ROS)[8]. Phagosomes must degrade pathogens efficiently to prevent them from
37 escaping. Many pathogens, such as the bacterium *Legionella pneumophila*, were found to evade the
38 degradative environment in phagosomes by hijacking the intracellular trafficking process[9, 10, 11].
39 These examples highlight that the degradative function of phagosomes is tightly associated with
40 their dynamics in cells. Understanding the relationship between the degradative function and
41 dynamics of phagosomes is critical for developing therapeutics against infections and
42 inflammation. It is, however, challenging due to the autonomous nature of the two processes. Each
43 phagosome degrades its cargo at its own distinct kinetic rate, which was assumed to be stochastic.
44 The velocity at which phagosomes are transported along microtubules is also heterogeneous and
45 believed to be stochastic[2, 12]. Therefore, those dynamic and biochemical changes must be quantified
46 at the single phagosome level to reveal their relationships, but there is currently no method to do
47 so. The dynamics of phagosomes in cells has been extensively studied using single-particle
48 imaging[13, 14]. The degradative activities, including lumen acidification and protein digestion, in
49 phagosomes have been studied separately in population-based measurements[15]. In those ensemble-
50 average studies, the individuality of phagosomes was overlooked. Regarding the relationship

between the degradative function and dynamics of phagosomes, studies have relied on approaches that inhibit phagosome dynamics by disrupting the cytoskeleton or molecular motor functions. The disruption of actin was shown to attenuate phagosome-endosome fusion[16, 17, 18]. Microtubule depolymerization was found to disrupt: i) phagosome-lysosome fusion[19], ii) content delivery from late endosomes to phagosomes[20], and iii) acquisition of lysosome markers[21]. These observations demonstrated that dynamics of phagosomes in cells is important for their degradative function, but none of those studies identified the quantitative relationship between phagosome dynamics and kinetics of the biochemical activities during cargo degradation.

In this study, we develop a single-phagosome imaging toolset for monitoring both degradative function and dynamics of individual phagosomes. The RotSensor particles are optically anisotropic and fluorogenic in response to acidification in phagosomes and phagosome-lysosome fusion, two key degradative activities. Using the RotSensors as cargos in phagosomes, we imaged simultaneously the biochemical changes during phagosome degradation and their translational and rotational dynamics in living cells. By combining this toolset with magnetic tweezers to control the dynamics of phagosomes, we obtained direct evidence that the microtubule-based centripetal transport of phagosomes determines the kinetic rates of their degradation process. More mobile phagosomes fuse with lysosomes and acidify in their lumen more rapidly, following a nearly linear relationship. Our results reveal the orchestration of the dynamical and biochemical processes that occur during pathogen degradation in phagosomes, providing a possible mechanism by which some pathogens may evade immune clearance by disrupting the intracellular dynamics of residing phagosomes.

## Results

75 **pH-responsive rotational particle sensors (pH-RotSensors) for measuring phagosome**
76 **acidification and dynamics**

77 The acidification of phagosome lumen is an early indicator of its degradative function and required
78 for many subsequent events, including the activation of degradative enzymes[22, 23]. Therefore, we
79 first designed pH-responsive RotSensors to simultaneously measure the acidification of single
80 phagosomes and their intracellular transport dynamics, including both translational and rotational
81 movements (Fig. 1a). Each RotSensor consists of a pH-responsive particle (1 μm diameter)
82 covalently conjugated with a smaller green particle (100 nm diameter) with non-overlapping
83 fluorescence emission (Fig. 1b). Once engulfed into phagosomes, the "snowman"-like RotSensors
84 report both the translational and the rotational motion of the residing phagosome. The azimuthal
85 (φ) and polar (θ) angles of each RotSensor can be measured, respectively, from the orientation and
86 projection distance between the pair of the two particles, as previously described (Fig. 1b)[24].
87

88 To monitor phagosome acidification, the 1 μm particle in each RotSensor was biotinylated and
89 subsequently conjugated with two types of streptavidin, one type labeled with the pH-indicator
90 pHrodo Red and the other with the reference dye CF640R. The dye pHrodo Red fluoresces intensely
91 in an acidic environment, making it an ideal indicator of phagosome acidification. CF640R was
92 chosen as a reference dye because it is pH insensitive and photostable (Supplementary Fig. 1).
93 Streptavidin is critical in the RotSensor design because it acts as a cushion layer to separate the
94 pHrodo Red dye from the particle surface. Without the streptavidin linker, pHrodo Red that was
95 directly conjugated onto the particle surface exhibited little pH sensitivity. The pH-sensitive
96 RotSensors were then coated with immunoglobulin G (IgG) via non-specific adsorption to initiate
97 Fc receptor (FcR)-dependent phagocytosis in RAW264.7 macrophage cells.
98

99 To quantify the pH response of the RotSensors, we measured the ratio of fluorescence emission
100 intensities of pHrodo Red and of the reference dye CF640R; $I_{pHrodo}/I_{ref}$, as we varied pH inside
101 phagosomes in live cells and in aqueous buffers (Supplementary Fig. 2). For both cases, $I_{pHrodo}/I_{ref}$
102 of the RotSensors increased linearly with decreasing pH, consistent with previous reports[25]. The pH
103 responses of individual RotSensors, including the initial $I_{pHrodo}/I_{ref}$ ratio and slope, varied slightly
104 from one to another, because of the different amounts of dyes on particles and the slightly different
105 phagosome lumen environments[26, 27, 28, 29]. To eliminate the effect of such variation in pH
106 measurements, we calibrated our pH measurements for each phagosome. We measured
107 $I_{pHrodo}/I_{ref}$ of each phagosome versus time and then converted the intensity ratio to pH based on
108 $I_{pHrodo}/I_{ref}$ of the same phagosome at pH 4.5 and 7.3 (details in Methods section).
109

110 **pH-RotSensors reveal correlation between phagosome acidification rate and transport**
111 **dynamics**

112 Before tracking the dynamics of phagosomes, we first asked whether the rotation of RotSensors
113 faithfully reports the rotation of their residing phagosomes. Transmission electron microscopy
114 (TEM) images show that ≈ 86% of internalized RotSensors remained tightly wrapped by the
115 phagosome membrane at the end of our experiments (50 min after particles were added to cells)
116 (Supplementary Fig. 3). Based on the tight membrane fitting and the presence of ligand-receptor
117 binding between the RotSensors and phagosome membranes, the RotSensors are unlikely to
118 freely rotate inside phagosomes. Thus, their rotation is expected to report the rotation of their
119 residing phagosomes.
120

121 We then simultaneously imaged the pH response and the rotational and translational dynamics of
122 single phagosomes encapsulating RotSensors (Fig. 1c). Phagosomes acidified in three steps: 1) an
123 initial standby period during which the phagosome pH remained at neutral pH of ≈ 7.3 (Fig. 1d),

124 2) a rapid acidification period when the pH quickly dropped over a period of a few minutes, and 3)
125 an eventually plateau at pH 4.5-5.0. This acidic pH is a prerequisite for activating degradative
126 enzymes[8, 30]. While individual phagosomes reached slightly different final pH values, their
127 acidification kinetics mostly (31 of 42 phagosomes) followed a sigmoidal-Boltzmann function:

128 $$pH = pH_{final} + \frac{pH_{initial} - pH_{final}}{1 + exp\,(\frac{t - t_0}{dt})} \quad (1)$$

129 in which $t_0$ is the half-response point, and $t_{initial}$ and $t_{final}$ denote the beginning and the end of
130 rapid acidification, respectively (Fig. 1d). Slope at $t_0$ is the acidification rate by definition. We
131 found that phagosomes acidified at an average rate of 0.33 ± 0.28 pH unit/min (N = 42). The
132 acidification of phagosomes requires intact microtubules, as the acidification was abolished upon
133 microtubule disruption by nocodazole (Supplementary Fig. 4).
134
135 For transport dynamics, we observed that a majority (~70%) of phagosomes exhibited a slow-to-
136 fast movement transition both translationally and rotationally (Fig. 1e and f). The remaining 30%
137 of phagosomes exhibited only slow movements. This initially slow movements are not dependent
138 on microtubules, as the average velocities were not affected by microtubule depolymerization
139 (Supplementary Fig. 5). After a few minutes of slow movements, phagosomes moved rapidly
140 centripetally with velocities as high as 0.1 μm/s (Fig. 1e). This range of phagosome velocities is
141 consistent with literature reports for 1 μm bead-containing phagosomes in macrophage cells[13].
142 Meanwhile, phagosomes also rotated frequently in between segments of translational motion with
143 rotational velocities up to 0.15 rad/s (Fig. 1f). These dynamic behaviors, particularly phagosome
144 rotation, are characteristic of cargo transport driven by microtubule-based molecular motors, as we
145 previously reported[31]. This was further confirmed in control experiments, in which the rapid
146 translational and rotational dynamics disappeared in cells treated with nocodazole (Supplementary
147 Fig. 4).
148

149 Notably, the beginning of the rapid acidification period appeared to coincide with the onset of fast
150 microtubule-based transport (Fig. 1e and f). To explore the possible correlation between the two
151 processes, we calculated the acidification rate of single phagosomes based on the sigmoidal fitting
152 of their individual pH-time plots (Fig. 1d). We then plotted the acidification rate of single
153 phagosomes against their individual translational and rotational velocities during the rapid
154 acidification phase (from $t_{initial}$ to $t_{final}$) (Fig. 1g and h). The acidification rate varied broadly
155 among phagosomes, even those from the same cells. This reflected the individuality of each
156 phagosome in degradation. Despite this heterogeneity, the acidification rates of individual
157 phagosomes follow a linear relationship with both their translational and rotational velocities with
158 a Pearson's coefficient of 0.78 and 0.81, respectively. Those observations apply not only to
159 phagosomes from different cells but also to those from the same cells. This is shown in Fig. 1g and
160 h, in which data of phagosomes from the same cells are the same color. This is also a general
161 phenomenon independent of the activation status of macrophage cells (Supplementary Fig. 6).
162
163 Further, the acidification rates of single phagosomes also follow a linear relationship with the
164 percentage, maximum amplitude, and frequency of active rotation of phagosomes during the rapid
165 acidification phase (from $t_{initial}$ to $t_{final}$) with a Pearson's coefficient of 0.76, 0.60 and 0.61,
166 respectively (Fig. 1i and j, and Supplementary Fig. 7). For this analysis, active rotation of
167 phagosomes was distinguished from passive random rotation by using a Wavelet analysis method
168 reported previously (Supplementary Fig. 8; Methods)[32]. The percentage of active rotation was
169 defined as the total time during which the phagosome underwent active rotation divided by the time
170 duration of its rapid acidification (from $t_{initial}$ to $t_{final}$). The results altogether indicate that more
171 mobile phagosomes acidify faster. As an additional evidence supporting this conclusion, we also
172 observed that the ~30% of phagosomes that never underwent rapid microtubule-based transport
173 exhibited minimal acidification (Supplementary Fig. 19a-c). Surprisingly however, the final pH

174 attained by individual phagosomes showed no correlation with either the translational or the
175 rotational velocities of those phagosomes (Supplementary Fig. 10). Because the final acidic pH
176 determines whether a phagosome can successfully degrade its cargo, this result suggests that the
177 degradative capacity of a phagosome is likely determined prior to its transport on microtubules, but
178 that the rate of degradation is correlated with the transport dynamics.

179

180 **FRET-RotSensors for measuring phagosome-lysosome fusion**

181 During cargo degradation, phagosome acidification relies on its continuous fusion with lysosomes,
182 which deliver proton-pumping vacuolar H+-ATPase (V-ATPase) to it[28, 33, 34, 35, 36]. Since we found
183 that more mobile phagosomes acidify more rapidly, we asked whether phagosome-lysosome fusion
184 is likewise correlated with phagosome mobility. To do this, we measured the kinetics of
185 phagosome-lysosome fusion by modifying the RotSensor design into a Förster Resonance Energy
186 Transfer (FRET)-based assay. This fluorescence assay can be used to determine when two
187 fluorophores, a donor inside lysosomes and an acceptor inside phagosomes, are in close proximity
188 to one another. FRET-sensitive RotSensors were prepared in the same way as pH-sensitive
189 RotSensors, but, in this case, the sensor particles were labeled with streptavidin that was conjugated
190 with the donor fluorophore Alexa568 (Fig. 2a). For FRET, lysosomes were loaded with fluid-phase
191 biotinylated bovine serum albumin (BSA) that was conjugated with the acceptor fluorophore
192 Alexa647 using a pulse–chase procedure[37]. We confirmed that the BSA-Alexa647-biotin was
193 contained inside lysosomes based on its colocalization with the lysosome marker LysoTracker
194 inside cells (Supplementary Fig. 11). Inside lysosomes, BSA-Alexa647-biotin was fragmented by
195 proteases before RotSensors were added to cells for internalization (Supplementary Fig. 12). The
196 working principle of the FRET assay is that once the contents of lysosomes are intermixed with the
197 phagosome lumen during fusion, the fragmented BSA-Alexa647-biotin from lysosomes will in
198 close proximity with Alexa568 conjugated RotSensors leading to FRET. The magnitude of the

199 FRET signal thus indicates the extent of phagosome-lysosome fusion. This assay doesn't
200 necessarily require biotin-streptavidin binding. We showed in *in vitro* experiments that FRET can
201 occur when BSA-Alexa647, without biotinylation, was added to FRET-RotSensors in 1xPBS
202 solution (Supplementary Fig. 13). However, we still used BSA-Alexa647-biotin in this FRET assay
203 because it was loaded into lysosomes much more efficiently than BSA-Alexa647 alone, which
204 improved the sensitivity of the FRET assay (Supplementary Fig. 14). The observation that the biotin
205 moiety promotes uptake of BSA by cells is consistent with previous reports[38, 39].
206
207 For a thorough validation of the FRET assay, we first tested the FRET-RotSensors *in vitro* by
208 mixing them with BSA-Alexa647 in 1xPBS (Supplementary Fig. 13). In this experiment, we could
209 not measure the acceptor emission in the FRET channel due to the excessive amount of free BSA-
210 Alexa647 in solution. Instead, we quantified the percentage of donor quenching as an indirect
211 indicator of FRET efficiency. We found that the percentage of donor quenching, first increased
212 linearly as a function of BSA-Alexa647 concentration in the lysosome loading solution ([BSA-
213 Alexa647]$_{loading}$), but reached a plateau at [BSA-Alexa647]$_{loading}$ > 200 μg/ml. This plateau indicates
214 the maximum FRET efficiency which is determined by the amount of the donor fluorophore
215 (Alexa568) available on RotSensors. For the FRET assay to accurately detect continuous fusion of
216 a phagosome with lysosomes, the concentration of acceptor fluorophores (Alexa647) loaded into
217 lysosomes must be optimized to achieve sufficient FRET efficiency without saturating the donor
218 on the RotSensors. We did this by optimizing the loading concentration of BSA-Alexa647-biotin
219 into lysosomes.
220
221 We next tested and optimized the FRET assay in live cells. To start with, we loaded lysosomes
222 using 10 μg/mL BSA-Alexa647-biotin ([BSA-Alexa647-biotin]$_{loading}$ = 10 μg/mL). After
223 internalization of FRET-RotSensors, lysosomes docked on the phagosomes, and the FRET-

224 RotSensors inside phagosomes exhibited decreased fluorescence emission in the donor channel
225 (ex/em: 561/586 nm) and simultaneously increased emission in FRET channel (ex/em: 561/680
226 nm) (Fig. 2b and c). For quantification, we calculated FRET ratio defined as:

227 $$FRET\ ratio = \frac{FRET_{em}}{AF568_{em}} = \frac{FRET_0 - \alpha \times AF568_{em} - \beta \times AF647_{em}}{AF568_{em}} \quad (2)$$

228

229 In this equation, $FRET_0$ is the measured FRET signal (ex/em 561/680 nm) before correction for
230 spectral bleed-through, $AF568_{em}$ is the emission in the donor channel (ex/em 561/586 nm), and
231 $AF647_{em}$ is the emission in the acceptor channel (ex/em 660/680 nm). The coefficient $\alpha$ corrects
232 the bleed-through contribution from the donor (Alexa568) due to the overlap of the donor emission
233 in the FRET channel. The coefficient $\beta$ corrects the non-FRET bleed-through from the acceptor
234 (Alexa647) due to the excitation of the acceptor at the donor excitation wavelength. Correction
235 factors $\alpha$ and $\beta$ were determined independently for each experiment (see Methods). Simultaneous
236 with the observation of lysosome docking on phagosomes, the FRET ratio of single phagosomes
237 increased continuously with time until it reached a plateau, following a sigmoidal relationship (Fig.
238 2d). This is a general phenomenon confirmed in over 40 phagosomes from 22 cells (Supplementary
239 Fig. 15a-c). The gradual increase in FRET ratio as a function of time indicates an increasing
240 concentration of acceptors (Alexa647) in phagosomes resulted from their continuous fusion with
241 lysosomes. FRET signal was diminished when microtubules were disrupted by nocodazole
242 treatment, which further confirms that this assay measures phagosome-lysosome fusion
243 (Supplementary Fig. 16).

244

245 We then asked: what caused the plateau in the FRET ratio of single phagosomes? This is unlikely
246 to be caused by the completion of phagosome-lysosome fusion, because lysosomes were seen to
247 dock on phagosomes after the FRET ratio reached its plateau. We explored two possible causes for
248 the plateau seen in the FRET ratio vs. time plots. One is that the concentration of acceptor

249 fluorophores delivered into phagosomes by lysosome fusion reached the threshold needed to
250 saturate the donor fluorophores on RotSensors. The second is that the acceptor concentration in the
251 phagosome had reached equilibrium with that in the lysosomes that were fusing with it. Even as
252 more lysosomes continued to fuse with the phagosome, the content exchange would no longer
253 increase the concentration of acceptors in the phagosome. To determine which of these two possible
254 circumstances caused the FRET ratio to plateau, we varied $[\text{BSA-Alexa647-biotin}]_{\text{loading}}$ from 2.5
255 μg/mL to 25 μg/mL (note: concentrations higher than 25 μg/mL resulted in decreased cell viability).
256 While the exact concentration of acceptors (Alexa647) inside lysosomes is unknown, it is
257 proportional to $[\text{BSA-Alexa647-biotin}]_{\text{loading}}$ (Supplementary Fig. 14 and Supplementary Fig. 15a-
258 c). The rationale here is that if the plateau in FRET ratio was caused by the saturation of donors on
259 RotSensors, the magnitude of plateau would be determined by the amount of donors on RotSensors
260 and thus should not change with $[\text{BSA-Alexa647-biotin}]_{\text{loading}}$. On the contrary, if the plateau of
261 FRET ratio occurred because the acceptor concentration reached an equilibrium between the
262 phagosome and fusing lysosomes, the magnitude of plateau would be determined by the acceptor
263 concentration inside lysosomes and thus should increase with $[\text{BSA-Alexa647-biotin}]_{\text{loading}}$. In
264 experiments, we found that the plateau level of FRET ratio increased with [BSA-Alexa647-
265 $\text{biotin}]_{\text{loading}}$ from 2.5 to 25 μg/mL (Supplementary Fig. 15a-d). This indicates that the FRET ratio
266 plateau was due to the establishment of equilibrium between the phagosome lumen and lysosomes,
267 and not saturation of donors on RotSensors.
268
269 We further optimized $[\text{BSA-Alexa647-biotin}]_{\text{loading}}$ to minimize cell-to-cell variation in loading
270 BSA-Alexa647-biotin into lysosomes. We found that the higher $[\text{BSA-Alexa647-biotin}]_{\text{loading}}$, the
271 more variation in the amount of BSA-Alexa647-biotin loaded into lysosomes between cells
272 (Supplementary Fig. 14). As a result, the plateau level of FRET ratio had larger variations at [BSA-
273 $\text{Alexa647-biotin}]_{\text{loading}} > 10$ μg/mL (Supplementary Fig. 15d). To estimate how the cell-to-cell

274 variation affects the measurement of phagosome-lysosome fusion kinetics, we normalized the
275 FRET ratio vs. time plot of each phagosome to its plateau level and then from the sigmoidal
276 Boltzmann fitting of each FRET ratio plot, we calculated the slope at half-response point $t_0$ as the
277 kinetic rate of phagosome-lysosome fusion (referred to as FRET rate) (Fig. 2d and Supplementary
278 Fig. 15e). In the FRET rate vs. $[\text{BSA-Alexa647-biotin}]_{\text{loading}}$ plot (Supplementary Fig. 15f), the
279 standard deviation of FRET rate between phagosomes increased significantly at $[\text{BSA-Alexa647-}$
280 $\text{biotin}]_{\text{loading}} > 10$ μg/ml. All results suggest that an optimal range of $[\text{BSA-Alexa647-biotin}]_{\text{loading}}$
281 for the FRET assay is ≤ 10 μg/ml. We therefore chose to use 10 μg/ml, the highest concentration
282 within this range, to improve the sensitivity of the FRET assay.
283

284 **FRET-RotSensors reveal correlation between phagosome-lysosome fusion kinetics and**
285 **phagosomes centripetal transport**

286 After the validation and calibration of the FRET fusion assay, we then investigated whether the
287 kinetics of phagosome-lysosome fusion (measured as the FRET rate) correlates with the motility of
288 phagosomes. Much like the heterogeneity in acidification, the FRET rate differed greatly between
289 phagosomes even within the same cell (Fig. 2e and f). However, all single phagosome FRET ratio
290 data follow a linear correlation with the translational and rotational velocities of phagosomes, with
291 a Pearson's coefficient of 0.75 and 0.86, respectively (Fig. 2e and f). This indicates that phagosomes
292 that moved faster translationally and rotated more along microtubules also fused more rapidly with
293 lysosomes.

294 Because lysosomes in macrophages are more concentrated in the perinuclear region (Fig. 3a)[40], we
295 then asked if, besides velocity, the direction of phagosome transport plays any role in their fusion
296 with lysosomes. To identify centripetal towards cell nucleus, we analyzed the distance of each
297 phagosome from the center of cell nucleus as a function of time (Fig. 3b). The effective transport
298 distance of a phagosome (grey shaded areas in Fig.3b) is the distance from the time when it begins

299 to fuse with lysosomes to the time when it reaches the nucleus boundary. The starting time of
300 phagosome-lysosome fusion was obtained from the sigmoidal fitting of the FRET ratio vs. time
301 plot (Fig. 2d). We also identified segments of active centripetal motion following a previously
302 reported method (Fig. 3b)[13]. Most phagosomes moved centripetally (Supplementary Fig. 17), but
303 not all of them exhibited active centripetal runs (Fig. 3b). As shown in Fig. 3A, phagosome #1
304 underwent a few segments of active centripetal runs, but phagosome #2 did not. Concurrently,
305 phagosome #1 also fused with lysosomes more rapidly (Fig. 3c). To confirm the generality of this
306 result, we quantified the centripetal velocity and percentage of active centripetal runs of single
307 phagosomes. Centripetal velocity was calculated as the effective transport distance divided by time.
308 The percentage of active centripetal run was calculated as the sum of time of all active centripetal
309 runs divided by the total duration of the effective transport (N = 40 phagosomes from 22 cells). The
310 results demonstrate that phagosomes with larger centripetal velocity and higher percentage of active
311 centripetal movements fuse faster with lysosomes (Fig. 3d).

312

313 **MagSensors for magnetic manipulation and imaging of phagosomes**

314 To determine whether the centripetal motility of phagosomes determines their fusion with
315 lysosomes and consequently their acidification, we applied magnetic tweezers to manipulate the
316 intracellular transport of single phagosomes. We simultaneously measured changes in phagosome
317 degradation (Supplementary Fig. 18). We designed 1 μm magnetically modulated phagosome
318 sensors (MagSensors) that were also pH-responsive (Fig. 4a). The MagSensors were biotinylated
319 and conjugated with SAv-pHrodo Red (pH indicator) and SAv-CF640 (reference), using the same
320 procedure as for the preparation of RotSensors. The MagSensors exhibited similar pH responses
321 (Supplementary Fig. 19). In all experiments, a solenoid tip was positioned on the opposite side of
322 the cell from the phagosome of interest, so that the phagosome could be pulled by magnetic
323 attraction from the cell periphery towards the center. The magnetic force exerted on individual

MagSensors was calibrated by tracking the movement of particles in a polydimethylsiloxane (PDMS) base calibration medium under magnetic pulling force. The magnetic force changes with the distance between the MagSensor and the solenoid tip following theoretical predictions (Fig. 4b)[41]. On average, the solenoid tip was positioned ≈ 43 μm from the MagSensor of interest. This means that the average force exerted on a MagSensor by the tip was ≈ 21 pN at the beginning of manipulation and reached as high as ≈ 31 pN as it moved closer to the tip at the end of imaging (Supplementary Fig. 20).

We performed the magnetic experiments in resting macrophages stably expressing actin-GFP (Supplementary Fig. 21). The fluorescence from actin-GFP allowed us to identify when phagosome formation completes[42, 43], so that we can apply magnetic pulling force on the MagSensor-containing phagosomes only after their internalization. We used resting cells for these experiments because they are less flat, which allows for better magnetic manipulation of the phagosome. The acidification-motility correlation of phagosomes in resting cells was similar to that in activated cells (Supplementary Fig. 6). In the experiments, we turned on the magnetic force immediately after the MagSensors were internalized into phagosomes, which was indicated by the actin-GFP intensity peak, and pulled the MagSensor-containing phagosomes from the cell periphery towards the center (Fig. 4a). The magnetic force remained on throughout imaging. Under the magnetic pulling force, phagosomes moved towards the magnetic tip with accelerated translational velocity and larger mean square displacements (Fig. 4d and Supplementary Fig. 22). Their trajectories were zigzagged (Fig. 4c), likely because the magnetic force applied on the MagSensors was only slightly larger than the collective forces from the microtubule-based molecular motors. As mentioned above, the magnetic pulling force on single MagSensors was ≈ 21 to 31 pN (Supplementary Fig. 20). For comparison, microtubule-based molecular motors were shown to exert collective forces as high as ≈ 20 pN on vacuoles encapsulating 1 μm particles[44]. Therefore, the zigzagged movements of

349 phagosomes are plausibly a result of the combined influence of the magnetic force and the forces
350 exerted by molecular motors. As the translational velocity of phagosomes accelerated under
351 magnetic pulling, they also acidified more rapidly (Fig. 5a). Phagosomes that were magnetically
352 pulled acidified at an average rate of 0.79 ± 0.54 pH unit/min (N = 38). In contrast, for phagosomes
353 not subject to magnetic pulling, an average rate of 0.48 ± 0.34 pH unit/min was observed (N = 33)
354 (Fig. 5b). Surprisingly, magnetic manipulation had no effect on the final pH of the phagosomes, as
355 phagosomes with or without magnetic manipulation reached an average final pH of 4.7 ± 0.4 and
356 4.7 ± 0.3, respectively (Fig. 5c). These results evidently demonstrate that faster transport of
357 phagosomes causes their faster acidification.
358
359 We next investigated how magnetic pulling affects phagosome-lysosome fusion using the FRET
360 fusion assay shown in Fig. 2. BSA-Alexa647-biotin (10 μg/ml) was used to load lysosomes. As
361 shown in Fig. 5c, the FRET signals from magnetically pulled phagosomes (average from N = 20
362 each) were noticeably more intense and increased more rapidly, indicating enhanced phagosome
363 fusion with lysosomes. The FRET rate, which indicates the phagosome-lysosome fusion kinetic
364 rate, is 0.28 ± 0.21 a.u. (N = 20) for phagosomes under magnetic pulling, in contrast to the average
365 rate of 0.15 ± 0.07 a.u. without magnetic forces (N = 20) (Fig. 5e). To investigate whether the
366 movement of phagosomes alone is sufficient to facilitate productive fusion with lysosomes, we next
367 treated cells with nocodazole, which disrupts microtubule-based transport of both phagosomes and
368 lysosomes. We then magnetically moved phagosomes the same way as in non-treated cells. Despite
369 the fast movement of phagosomes under magnetic pulling forces, they exhibited minimal fusion
370 with lysosomes and minimal acidification (Supplementary Fig. 23). This suggests that productive

371 phagosome-lysosome fusion requires active transport of not only the phagosomes but also the
372 lysosomes that they fuse with.
373
374 The magnetic tweezers results, taken together, demonstrate that faster transport of phagosomes on
375 microtubules promotes their encounters with lysosomes, which leads to faster acidification. This
376 explains why phagosome transport velocity positively correlates with phagosome-lysosome fusion
377 kinetics and acidification rate.
378

379 **Discussion**

380 Phagosomes, even those from the same cells, show a significant amount of variation from one
381 another in their degradation and transport. Each phagosome functions as a separate degradative unit
382 with its own distinct degradation kinetics and transport velocity. However, the individuality of
383 phagosomes has been overlooked in previous studies that relied on population-based measurements
384 of phagosomes[8, 30, 45, 46]. There is no known quantitative relationship between the seemingly
385 stochastic rates of degradation of single phagosomes and their equally stochastic transport
386 dynamics. In the current study, we detail the development of a single-phagosome imaging and
387 manipulation toolset that allowed us to probe both degradative processes and dynamics of
388 individual phagosomes. Multimodal particle sensors, called RotSensors, were engineered as
389 phagosome probes to measure acidification within the lumen of an individual phagosome, the
390 kinetics of that same phagosome's fusion with lysosomes, and its overall rotational and translational
391 motion within the cell. The RotSensors were further combined with magnetic tweezers to perturb
392 phagosome transport and observe the consequences for the degradation of single phagosomes. This
393 integrated approach allowed us to demonstrate that the biochemical progression of degradative
394 functions in individual phagosomes is coupled to and determined by the dynamics of their active
395 transport.

396

397 By simultaneously tracking the transport dynamics and degradation of single phagosomes, we first
398 determined that phagosomes that move faster centripetally fuse with lysosomes and acidify faster.
399 While phagosome degradation is known to require microtubule-dependent transport[19, 21, 33, 47, 48, 49,
400 50, 51], our results demonstrate that the seemingly stochastic rate of degradation of single phagosomes
401 is positively correlated with their equally stochastic velocity of transport. In the magnetic tweezers
402 experiments, we then showed that when phagosomes are accelerated towards nucleus, they speed
403 up their fusion with lysosomes and their acidification. The velocity of phagosomes directly
404 regulates where and how fast they fuse with lysosomes, and this, in turn, determines the
405 acidification. Surprisingly however, phagosome velocity doesn't influence the final pH of the
406 phagosomes. Our results suggest that centripetal transport of phagosomes functions as a clock that
407 determines the timing of their sequential biochemical activities during pathogen degradation. The
408 precise positioning of phagosomes largely relies on microtubules-based motors[52]. It was shown
409 previously that Rab7-RILP (Rab7-interacting lysosomal protein) complex induces the recruitment
410 of the dynein-dynactin motor protein complex to phagosomes[53], and the clustering of dynein
411 generates extra force to mediate the rapid centripetal transport of phagosomes towards the
412 perinuclear region[50]. Because lysosomes are enriched in perinuclear region (Fig. 3a) and the
413 perinuclear lysosomes are more acidic than those near cell periphery[54, 55] , it is possible that dynein-
414 mediated active centripetal transport enhances the probability of physical collision between a
415 phagosome and lysosomes, hence promoting the degradation of phagosome lumen. We further
416 confirmed that it is the active microtubule-based centripetal transport, rather than simple diffusion,
417 regulates phagosome degradation. Because phagosomes failed to fuse with lysosomes or to acidify
418 in cells with disrupted microtubules, even if phagosomes were moved magnetically. Moreover,
419 Rab7 not only bridges phagosomes with dynein-dynactin, but also directly recruits the homotypic
420 fusion and vacuole protein sorting (HOPS) complex and V-ATPase subunit V1G1, which are

421 involved in membrane fusion and phagosome acidification[56, 57]. Those literature reports, albeit
422 scattered, suggest that phagosome membrane associated molecules, such as Rab7-RILP complexes,
423 may function as the molecular links that relate phagosome motility with their degradation activities.
424
425 In addition to studying phagosomes, we envision that the RotSensor toolset presented here could
426 be further applied, with appropriate modifications, to studying intracellular pathogens and
427 endosome degradation. Many pathogens, such as the bacterium *Legionella pneumophila*, hijack the
428 phagosome-lysosome fusion process to evade immune clearance[9, 10, 11]. Our study here was done
429 with synthetic beads, which are far less complex than pathogens. Nevertheless, the results imply
430 that intracellular pathogens might prolong their survival in host cells by disrupting the intracellular
431 transport of phagosomes to slow down fusion with lysosomes and thus delay the degradation. This
432 hypothesis can be tested in future studies where pathogen-extracted bioparticles or intact pathogens,
433 instead of synthetic particles, can be used in the single-particle assays. Similarly, when smaller
434 nanoparticles are used to replace the micron-sized beads in the single-particle assays, it will be
435 possible to study the degradative function of endosomes that are smaller than phagosomes.
436
437 **Methods**
438 **Materials**
439 Carboxylate-modified yellow-green fluorescent polystyrene nanoparticles (diameter 100 nm),
440 carboxylate-modified superparamagnetic Dynabeads (diameter 1 μm), pentylamine-biotin, Alexa
441 Fluor 568 NHS ester (succinimidyl ester), Alexa Fluor 647 NHS ester (succinimidyl ester), pHrodo
442 iFL Red STP Ester, Streptavidin, LysoTracker Green DND-26, Alexa Fluor 488 anti-tubulin-α
443 antibody, Alexa Fluor Plus 647 phalloidin, and DQ-green BSA were purchased from ThermoFisher
444 (Waltham, MA). Immunoglobulin G from rabbit plasma, albumin from bovine serum (BSA), biotin
445 N-hydroxysuccinimide ester (biotin-NHS), nocodazole, and lipopolysaccharides were purchased

446 from Sigma-Aldrich (St. Louis, MO). Monodisperse amine-modified silica particles (diameter 1.0
447 μm) were purchased from Spherotech Inc. (Lake Forest, IL). Sylgard 184 PDMS base was from
448 Dow Corning (Midland, MI). 1-(3-Dimethylaminopropyl)-3-ethylcarbodiimide hydrochloride
449 (EDC) was purchased from Alfa Aesar (Haverhill, MA). Nigericin sodium salt was purchased from
450 Tocris Bioscience (Minneapolis, MN). Recombinant Murine IFN-γ was purchased from Peprotech
451 (Rocky Hill, NJ). CF640R-amine was purchased from Biotium (Fremont, CA). RAW264.7
452 macrophage was purchased from ATCC (Manassas, VA). RAW264.7 macrophages stably
453 expressing EGFP-actin have been previously described [42]. Ringer's solution (pH = 7.3, 10 mM
454 HEPES, 10 mM glucose, 155 mM NaCl, 2 mM $NaH_2PO_4$, 5 mM KCl, 2 mM $CaCl_2$, 1 mM $MgCl_2$)
455 was used for live-cell imaging. Potassium-rich solution (135 mM KCl, 2 mM $K_2HPO_2$, 1.2 mM
456 $CaCl_2$, 0.8 mM $MgSO_4$) was used for intracellular pH calibration. Acidic washing solution (135
457 mM KCl, 2 mM $K_2HPO_2$, 1.2 mM $CaCl_2$, 0.8 mM $MgSO_4$, 5 mM sodium citrate) at pH of 4.5 was
458 used for particle washing in the EDC coupling step of the RotSensor fabrication. Artificial lysosome
459 fluid (55 mM NaCl, 0.5 mM $Na_2HPO_4$, 0.26 mM trisodium citrate dihydrate, 0.79 mM glycine, 150
460 mM NaOH, 108 mM citric acid, 0.87 mM $CaCl_2 \cdot 2H_2O$, 0.27 mM $Na_2SO_4$, 0.25 mM $MgCl_2 \cdot 6H_2O$,
461 0.46 mM disodium tartrate, 1.6 mM sodium pyruvate) was prepared following a previously reported
462 protocol [58] and used for washing particles during the protein conjugation step of the RotSensor
463 fabrication.
464

465 **Cell Culture, Pharmacological Treatments**

466 Both RAW264.7 macrophage and stable cell line expressing EGFP-actin were cultured in
467 Dulbecco's Modified Eagle Medium (DMEM) complete medium supplemented with 10% fetal
468 bovine serum (FBS), 100 units/ml penicillin and 100 μg/ml streptomycin at 37°C and 5% $CO_2$.
469 Resting macrophages were activated with a combination of 50 ng/ml LPS and 100 units/ml IFN-γ
470 for 9 h prior to live cell imaging. Microtubule depolymerization was achieved by incubating cells

471 with 10 μM nocodazole for 1 h prior to imaging, and 10 μM nocodazole was presented during live
472 cell imaging.
473
474 **Fabrication and Characterization of Phagosome Sensors**
475
476 **(a) Fluorescence labeling of Streptavidin and Bovine Serum Albumin (BSA)**
477 To prepare streptavidin-pHrodo Red conjugates (SAv-pHrodo Red), 0.7 mg of streptavidin, 60 μg
478 of pHrodo Red STP Ester were mixed in 350 μl $NaHCO_3$ solution (100mM, pH 8.2) for 3 h at room
479 temperature. Free dyes were removed by centrifugal filtration using Amicon Ultra filters (30K). To
480 prepare streptavidin-CF640R conjugates (SAv-CF640), 0.7 mg of streptavidin, 80 μg of CF640R-
481 amine, and 3 mg of EDC were mixed in 350 μl MES buffer (50mM, pH 4.5) for 3 h at room
482 temperature. Free dyes were removed by centrifugal filtration using Amicon Ultra filters (30K). To
483 prepare streptavidin-Alexa568 conjugates (SAv-Alexa568), 0.5 mg of streptavidin, 60 μg of Alexa
484 Fluor 568 NHS ester were mixed in 235 μl $NaHCO_3$ solution (100mM, pH 8.2) for 1 h at room
485 temperature. Free dyes were removed by centrifugal filtration using Amicon Ultra filters (30K). To
486 prepare bovine serum albumin-Alexa647-biotin (BSA-Alexa647-biotin) conjugates, a mixture
487 containing 2 mg/ml BSA and 188 μg/ml (molar ratio of 1: 20) biotin-NHS in $NaHCO_3$ solution
488 (100 mM, pH 8.2) was incubated at room temperature for 1 h. Unbound biotin-NHS was removed
489 by centrifugal filtration using Amicon Ultra filters (30K). After washing, a mixture containing 2
490 mg/ml BSA-biotin and 780 μg/ml Alexa Fluor 647 NHS ester in $NaHCO_3$ solution (100 mM, pH
491 8.2) was incubated at room temperature for 3 h. Free dyes were removed by centrifugal filtration
492 using Amicon Ultra filters (30K). The resulting BSA-Alexa647-biotin yielded dye: protein ratios
493 of 1.2:1 on NanoDrop UV-Vis measurement (ThermoFisher, Waltham, MA). To prepare bovine
494 serum albumin-Alexa647 (BSA-Alexa647) conjugates, a mixture containing 2 mg/ml BSA and 780
495 μg/ml Alexa Fluor 647 NHS ester in $NaHCO_3$ solution (100 mM, pH 8.2) was incubated at room

496 temperature for 1 h. Free dyes were removed by centrifugal filtration using Amicon Ultra filters
497 (30K). The resulting BSA-Alexa647 yielded dye: protein ratios of 1.3:1 based on NanoDrop UV-
498 Vis measurement (ThermoFisher, Waltham, MA).
499

500 **(b) Fabrication of Rotational Phagosome Sensors (RotSensors)**

501 RotSensors: Amine-modified non-fluorescent silica particles (1 μm) were incubated with 150
502 μg/ml biotin-NHS in $NaHCO_3$ solution (10 mM, pH 8.25) for 2 h at room temperature and then
503 with 500 μg/ml of biotin-NHS for 30 min for a second round of biotinylation. After biotinylation,
504 silica particles were washed in methanol and deionized (DI) water. The "snowman"-like design was
505 introduced by covalently conjugating the carboxylate-modified yellow-green fluorescent
506 nanoparticles (100 nm) to the biotinylated and amine-modified silica particles (1 μm) using EDC
507 coupling. In brief, carboxylate-modified yellow-green fluorescent nanoparticles (100 nm) were
508 mixed with the biotinylated and amine-modified silica particles (1 μm) at a molar ratio of 333:1 in
509 phosphate buffer (10 mM, pH 7.0) containing 1.0 mg/ml EDC for 2 h at room temperature. After
510 the EDC coupling, particles were washed with acidic washing solution and 1×PBS to remove the
511 non-covalently bounded carboxylate-modified yellow-green fluorescent nanoparticles (100 nm).
512 20% of the particles were found to have the "snowman" shape with 1:1 coupling ratio of the
513 biotinylated and amine-modified silica particles (1 μm) and the carboxylate-modified yellow-green
514 fluorescent nanoparticles (100 nm).

515 pH-RotSensors: pH-RotSensors were fabricated by labeling RotSensors with SAv-pHrodo Red and
516 SAv-CF640. RotSensors were incubated with 25 μg/ml of SAv-pHrodo Red, 2.5 μg/ml of SAv-
517 CF640, 5 μg/ml of BSA and 1 μg/ml of IgG in 1×PBS for 5 h at room temperature. Unbound
518 proteins were rinsed off with artificial lysosome fluid and 1×PBS. The resulting pH-RotSensors
519 were further opsonized with 30 μg/ml IgG in 1×PBS for additional 2 h before adding to cell
520 samples.

521 FRET-RotSensors: FRET-RotSensors were fabricated by labeling RotSensors with SAv-Alexa
522 568. The RotSensors were incubated with 27.5 μg/ml of SAv-Alexa568, 5 μg/ml of BSA, and 1
523 μg/ml of IgG in 1×PBS for 5 h at room temperature. Unbound proteins were rinsed off with artificial
524 lysosome solution and 1×PBS. The FRET-RotSensors were further opsonized with 30 μg/ml of IgG
525 in 1×PBS for additional 2 h before adding to cell samples.

526

527 **(c) Fabrication of Magnetically Modulated Phagosome Sensors (MagSensors)**

528 pH-MagSensors: The first step is the biotinylation of carboxylate-modified Dynabeads (1 μm). In
529 brief, 10 μl of stock Dynabeads suspension (10 mg/ml) were added to 100 μl of MES buffer (50
530 mM, pH 6.2) containing 10 mg/ml EDC and 1 mM of biotin pentylamine. After 1-h incubation at
531 room temperature, biotinylated Dynabeads (1 μm) were washed in 1×PBS to remove unbound
532 biotin pentylamine. pH-MagSensors were fabricated by labeling biotinylated Dynabeads (1 μm)
533 with SAv-pHrodo Red and SAv-CF640. Biotinylated Dynabeads were incubated with 50 μg/ml of
534 SAv-pHrodo Red and 50 μg/ml of SAv-CF640 for 1 h at room temperature. The resulting pH-
535 MagSensors were further opsonized with 1 mg/ml of IgG in 1×PBS for additional 1 h before adding
536 to cell samples.

537

538 FRET-MagSensors: Biotinylated Dynabeads (1 μm) were prepared following the same procedure
539 described above. FRET-MagSensors were fabricated by labeling biotinylated Dynabeads (1 μm)
540 with SAv-Alexa568. Biotinylated Dynabeads were incubated with 27.5 μg/ml of SAv-Alexa568
541 for 1 h at room temperature. The resulting FRET-MagSensors were further opsonized with 1 mg/ml
542 of IgG in 1×PBS for additional 1 h before adding to cell samples.

543

544 **Magnetic Tweezers Setup and Force Calibration**

Magnetic tweezers were built on an inverted fluorescence microscope system (Nikon Eclipse Ti-U, Nikon, Tokyo, Japan), as shown in Supplementary Fig. 18. The setup mainly includes a solenoid and a power supply. The solenoid was assembled by inserting a high permeability HyMu-80 alloy rod (Carpenter Technology, Reading, PA) into an aluminum bobbin wrapped with 600 turns of copper coil [59] (Supplementary Fig. 18b). The tip of the rod has a diameter of ≈ 1 μm (Supplementary Fig. 18c). Position of the solenoid was controlled with a manual micromanipulator (Narishige NMN-21) to achieve independent control of its position in the x-, y-, and z-direction with a minimum graduation of 250 nm in the x-y plane and 1 μm in the z-direction. The current going through the solenoid was generated by a programmable power supply (Tekpower, Montclair, CA) with a maximum power output of 5 A.

Magnetic force was calibrated as a function of particle-to-tip distance by measuring the movements of Dynabeads (1 μm) in magnetic field. In brief, CF640R labeled Dynabeads (1 μm) were suspended in PDMS base at a concentration of ≈ $3.0 \times 10^5$ particles/ml. This low particle concentration was necessary to avoid particle aggregation and inter-particle magnetic inference [60]. The PDMS base, which has a high viscosity of 5.1 Pa·s, was chosen to slow down particle movements to make particle tracking feasible. The initial positions of the solenoid tip and of the magnetic particles were imaged in bright field before time-lapse epi-fluorescence images of particles were acquired with an interval time of 0.2 s. Working current of the magnetic tweezers was 1.0 A in the calibration. The magnetic force $F(r)$ exerted on each magnetic particles at particle-to-tip distance r was converted from particle velocity values using Stokes-Einstein equation:

$$F(r) = 3 \cdot \pi \cdot \eta \cdot d \cdot v, \quad (1)$$

where $\eta$ is the viscosity of calibration solution PDMS base, d represents the diameter of particle, and v is the velocity of particle. The relationship between magnetic force F(r) and particle-to-tip distance $r$ was fitted using equation:

$$F(r) = \frac{F_0}{[\frac{r}{2r_0}+\frac{1}{2}]^{C_F}}, \quad (2)$$

Where $F_0$ is a force constant with the unit of pN, $r_0$ is a distance constant with the unit of μm, $C_F$ is unitless and $F_{(r0)} = F_0$ [59].

**Fluorescence Microscopy**

**(a) Single-phagosome pH Assay**

RAW264.7 macrophage cells were seeded on glass coverslips at $2.0 \times 10^5$ cells/ml in complete medium for 24 h and then activated with LPS and IFN-γ following the procedure described above. For all single-phagosome pH studies, the recognition of pH-Sensors (i.e. pH-RotSensor and pH-MagSensor) by macrophages was synchronized following a previously reported protocol [61]. Briefly, cell samples were cooled on ice for 3 min to postpone phagocytosis. pH-Sensors were then added at a particle-to-cell ratio of ~5:1. Bindings of particles on macrophage were synchronized by centrifuging cell samples at 200×g for 30 s. Live cell imaging was conducted in Ringer's solution at 37°C on a Nikon Eclipse-Ti inverted microscope equipped with a 1.49 N.A. ×100 TIRF objective (Nikon, Tokyo, Japan) and an Andor iXon3 EMCCD camera (Andor Technology, Belfast, U.K.). Fluorescence emissions at three wavelengths (ex: 488, 561, and 660 nm; em: 515, 586 and 680 nm) were acquired for the time-lapse imaging. The acquisition rate was 2 sec/frame. Single-phagosome pH assay in actin-GFP expressing RAW264.7 macrophages was conducted following the same procedure described above.

592 **(b) Single-phagosome FRET-fusion Assay**

593 RAW264.7 macrophage cells were seeded on glass coverslips at $2.0 \times 10^5$ cells/ml in complete
594 medium for 24 h and then activated with LPS and IFN-γ following the procedure described above.
595 Loading of either BSA-Alexa647-biotin or BSA-Alexa647 into lysosome compartment was carried
596 out following a previously reported pulse-chase protocol [62, 63, 64]. In brief, RAW264.7 macrophage
597 cells were incubated overnight in complete medium containing either BSA-Alexa647-biotin or
598 BSA-Alexa647 at indicated concentration. 2 h prior to live cell imaging, cells were rinsed twice
599 with complete medium. Labeled endocytic compartment was then chased at 37°C for 2 h to ensure
600 complete accumulation and fragmentation of fluorescently labeled BSA in lysosome compartments
601 (Supplementary Fig. 11 and Supplementary Fig. 12). Synchronized internalization of FRET-
602 Sensors (i.e. FRET-RotSensor and FRET-MagSensor) was conducted following the same
603 procedure described above. Time-lapse epi-fluorescence images were acquired to record FRET
604 emission ($FRET_0$; ex/em 561/680 nm), donor emission ($Alexa568_{em}$; ex/em 561/586 nm), acceptor
605 emission ($Alexa647_{em}$; ex/em 660/680 nm) and the emission from 100 nm yellow-green
606 fluorescence particle (ex/em 488/515 nm). The acquisition rate was 4 sec/frame.

607

608 The broad emission spectra of Alexa568 (donor) overlap partially with the acceptor emission
609 channel (680 nm) and the broad excitation spectra of Alexa647 (acceptor) did overlap partially with
610 donor excitation channel (561 nm). This resulted in two types of spectral cross-talks: (i) the
611 detection of donor fluorophore (Alexa568) emission at acceptor emission channel (680 nm) under
612 the donor excitation of 561 nm and (ii) the detection of acceptor fluorophore (Alexa647) emission
613 at acceptor emission channel (680 nm) under the donor excitation of 561 nm in the absence of FRET
614 effect. These two cross-talks, however, are constant throughout FRET-fusion assay, and could be
615 deducted from the measured FRET emission ($FRET_0$) to obtain FRET-generated emission
616 ($FRET_{em}$). Correction factors $\alpha$ and $\beta$ for cross-talks were determined for each independent
617 experiment based on: (1) the measured FRET emission and donor emission of Alexa568

618 streptavidin particles outside cells and (2) the measured FRET emission and acceptor emission of
619 acceptor fluorophore (Alexa647) in cells without FRET-sensor. The FRET ratio is obtained as
620 follows:

621 $$FRET\ ratio = \frac{FRET_{em}}{AF568_{em}} = \frac{FRET_0 - \alpha \times AF568_{em} - \beta \times AF647_{em}}{AF568_{em}}, \quad (3)$$

622 where $FRET_0$ is the measured FRET emission (ex/em 561/680 nm) before cross-talk correction,
623 $FRET_{em}$ is the FRET emission, $AF568_{em}$ is the donor emission (ex/em 561/586 nm) and
624 $AF647_{em}$ is the acceptor emission (ex/em 660/680 nm). The FRET increase was gradual, not
625 stepwise, because multiple dye-loaded lysosomes can simultaneously fuse with a single phagosome
626 and the increment in FRET signal from a single phagosome-lysosome fusion is too small to be
627 resolved.

628

629 **(c) DQ-green BSA Digestion Assay**

630 To estimate the fragmentation level of BSA-Alexa647-biotin chasing, we loaded DQ-green BSA
631 into lysosome compartment following the same pulse-chase produced described above, and
632 measured the dequenching kinetics of lysosomal DQ-green BSA as a function of time. A DQ-green
633 BSA concentration at 50 μg/ml was used during pulse. After the overnight pulse, cells were rinsed
634 3 times with flour-free Ringer's solution and imaged using Epi-fluorescence microscope. The
635 emission of DQ-green (ex/em 488/515 nm) was recorded every 5 min for 2 h.

636

637 **(d) Immunofluorescence Staining and Imaging**

638 RAW 264.7 macrophages were seeded and activated as described above. For immunostaining of α-
639 tubulin and F-actin, cells were first washed with 1× PBS and fixed with 2% PFA at room
640 temperature for 5 min. Next, they were permeabilized with 0.1% Triton X-100 for 5 min at room
641 temperature, and blocked with 2% BSA for 1 h at room temperature. After the BSA blocking, cells
642 were incubated with 2 μg/mL Alexa Fluor 488 anti-tubulin-α antibody and 2 μg/mL Alexa Fluor

643 647 phalloidin for 1 h at room temperature. Super-resolution structured illumination microscopy
644 (SIM) images of the labeled cells were acquired using a DeltaVision OMX SR imaging system
645 equipped with a Olympus Plan Apo 60×/1.42 PSF objective and a sCMOS camera.
646
647 **(e) Lysotracker Labeling and Imaging**
648 RAW 264.7 macrophages were seeded and activated as described above. After overnight incubation
649 in complete medium containing 5 μg/mL BSA-Alexa647-biotin, the labeled endocytic
650 compartments were chased at 37°C for 1.5 h. Cells were then incubated with 50 nM Lysotracker
651 Green DND-26 at 37°C for 30 min. After that, cells were rinsed twice with Ringer's solution to
652 remove the free fluorophore and imaged using Re-scan Confocal Microscopy (RCM) equipped with
653 a 1.49 N.A. ×100 TIRF objective and ORCA-fusion CMOS camera.
654
655 **Image Analysis**
656
657 **(a) Image Registration**
658 Image registration was done to correct for the optical shift between different imaging channels. 100
659 nm TetraSpeck fluorescent particles (Ex/Em: 360/430 nm, 505/515 nm, 560/580 nm, and 660/680
660 nm) were adsorbed on poly-l-lysine-coated glass coverslips at a surface density of ≈ 0.10 bead/$\mu m^2$
661 and used as markers for image registration. After sequential imaging of the marker particles in three
662 channels (Ex: 488, 561, and 660 nm), an affine transformation was applied to align particle
663 localization maps from 488 and 660 nm channels (termed target images) to that from the 561 nm
664 channel (reference image) using ImageJ plugin MultistackReg [65]. A global mapping matrix was
665 obtained to record all the transformation steps and used to apply the same operations to all images.
666
667 **(b) Single-Particle Localization and Intensity Determination**

668 The centroids of single particles in epi-fluorescence images were localized using a Gaussian-based
669 localization algorithm in the ImageJ plugin Trackmate. To measure the emission of CF640R and
670 pHrodo Red on pH-Sensors (i.e. pH-RotSensor and pH-MagSensor), pixel intensities within a
671 diameter of 2 μm from the localized centroid of the particle were integrated and background-
672 corrected using custom MATLAB algorithms. Same procedure was carried out for determining
673 $FRET_0$, $AF568_{em}$ and $AF647_{em}$ in single-phagosome FRET-fusion assay. To determine the
674 localization uncertainties, pH-RotSensors were immobilized on poly-l-lysine-coated glass coverslip
675 and imaged for 200 consecutive frames in Ringer's solution. Localization uncertainty was defined
676 as the standard deviation of the tracked particle positions in x- and y-coordinates. The localization
677 uncertainties of the 1 μm pHrodo Red-coated particle and 100 nm yellow-green fluorescence
678 nanoparticle were determined to be 20.6 ± 4.05 nm and 13.1 ± 2.32 nm, respectively
679 (Supplementary Fig. 25).
680

681 **(c) Translational and Rotational Tracking Analysis of RotSensors**

682 The single particle tracking analysis was done as described previously [24, 66]. Briefly, translational
683 velocity was determined from the centroid location of the 1 μm pHrodo Red- or SAv-Alexa568-
684 coated particle ($X_{red}$, $Y_{red}$) as a function of time. For rotational tracking, a vector was drawn from
685 the centroid of the 1 μm red fluorescent particle ($X_{red}$, $Y_{red}$) to that of the 100 nm yellow-green
686 nanoparticle ($X_{green}$, $Y_{green}$) belonging to the same RotSensor. Orientation of the vector was obtained
687 as the in-plane angle, $\varphi$, for the single RotSensor. The length of the vector was used to calculate
688 the out-of-plane angle, $\theta$, using the equation below:

689 $$\theta = arcsin\,(\frac{d}{r}), \quad (4)$$

690 where $d$ is the projection inter-particle distance between a pair of green and red dots in each given
691 image, and $r$ is the physical inter-particle distance. Because $r$ varies slightly from one particle to
692 another due to the size distribution, $r$ was obtained as the maximal projected inter-particle distance

693 $d_{max}$ when a RotSensor samples all possible orientations and the $d_{max}$ was larger than 550 nm. In
694 cases when $d_{max}$ < 550 nm, $r$ was set to 550 nm. Two-dimensional rotational velocity was
695 determined from the rotation matrix derived from $\varphi$ and $\theta$ at consecutive frames. Using this
696 method, φ can be measured within a full range (−180° to +180°), but there is ambiguity in measuring
697 θ, because RotSensors oriented at a polar angle of θ or (180° − θ) are indistinguishable from one
698 another when observed as a two-dimensional projection image. However, this ambiguity does not
699 affect the measurements of Δθ and translational velocity in this study, because Δθ of phagosomes
700 between consecutive image frames (2s/frame) is expected to be < 90°, based on the result that
701 phagosomes rotate an average Δφ of 0.12 ± 0.16 rad (6.9° ± 9.2°) between consecutive frames
702 (Supplementary Fig. 26). Therefore, only Δθ < 90° was used in the tracking analysis for calculating
703 rotational velocity of phagosomes.
704
705 **(d) Determination of Active Centripetal Run** The directional transport of phagosomes was
706 analyzed following a previously reported method with slight modification [13]. The centroid of the
707 nucleus was obtained based on bright field image of the cell (Supplementary Fig. 27) [48, 67]. At each
708 time point of a particle trajectory, the distances between the phagosome and the centroid of the
709 nucleus was quantified (referred to as 'distance-to-nucleus') (Fig. 4b). The travelled distance of
710 phagosome towards the nucleus was subdivided into segments with a length of 32 seconds. Each
711 segment was categorized as either a segment of active run or as a segment of passive motion based
712 on the travelled distance with regards to nucleus. The distance threshold for active run was set to
713 0.5 μm, independent of the direction of motion whether it is towards the nucleus (centripetal) or
714 towards the periphery (centrifugal) [68]. Finally, segments of active runs were classified either as
715 active centripetal run or as active centrifugal run depending on the directionality of the transport.
716
717 **(e) Intracellular pH Calibration**

718 The intracellular pH calibration of pH-RotSensors and pH-MagSensors was done following a
719 previously published protocol [26]. Macrophages seeded on glass coverslips were pretreated with 10
720 μM concanamycin in Ringer's solution for 10 min before the addition of particles and then
721 incubated at 37°C for 10 min to promote particle phagocytosis. Cell medium was replaced with
722 potassium-rich buffers at different pH values. All buffers contain 20 μM of nigericin, but different
723 buffering agent: 5 mM acetic acid for pH 4.5, 5 mM MES for pH 5.5, and 5mM HEPES for pH 6.5
724 and 7.3. The pH calibration was done from pH 7.3 to 4.5. For each pH, cells were rinsed twice with
725 the correspondingly buffer and allowed to equilibrate for 5-10 min before image acquisition.
726 Fluorescence emission of the pHrodo Red at 586 nm ($I_{pHrodoRed}$) and reference dye CF640R at
727 680 nm ($I_{ref}$) was obtained at various pH and background-corrected to obtain ratiometric pH
728 calibration plots (Supplementary Fig. 2).
729
730 In live cell imaging, pH calibration was done for individual internalized pH-RotSensors and pH-
731 MagSensors to eliminate the effect of particle-to-particle variation in their pH responses. By
732 plotting $I_{pHrodo}/I_{ref}$ vs. time for single phagosomes, we notice that acidification process started with
733 a standby period during which $I_{pHrodo}/I_{ref}$ ratio remains unchanged denoting that the phagosome pH
734 remained equivalent to extracellular pH of 7.3 (Ringer's solution, pH = 7.3) before the initiation of
735 phagosome acidification (Supplementary Fig. 28a and b). We further confirmed this by imaging
736 phagosome acidification in cells expressing actin-GFP, in which intensity peak of actin-GFP
737 pinpointed the time of particle internalization [42, 43] (Supplementary Fig. 28c-e). After live cell
738 imaging, the same cell sample was incubated in pH 4.5 potassium-rich pH calibration buffer
739 containing 20 μM of nigericin to obtain the ratiometric emission ($I_{pHrodo}/I_{ref}$) of the RotSensor
740 at pH 4.5 (Supplementary Fig. 28a). In the final step of the calibration procedure, a linear function
741 was generated based on the known $I_{pHrodo}/I_{ref}$ ratios at pH 4.5 and 7.3, and the result function

742 was used to transform the fluorescence measurements of the RotSensor to luminal pH values
743 (Supplementary Fig. 28b and f).
744
745 **(f) Wavelet Transform Analysis**
746 A wavelet analysis algorithm reported by Chen *et al*. was used to distinguish active rotation from
747 passive one. Both in-plane ($\theta$) and out-of-plane ($\varphi$) displacement of a RotSensor was convoluted
748 using the 1-dimensional Haar continuous time wavelet transform [32]. The wavelet coefficients after
749 the transformation were plotted as a function of time and for different widths of the wavelet function
750 (Supplementary Fig. 8). The width of the wavelet function used here is the number of image frames
751 and referred to as "scale". Scale 10 was chosen as a universal threshold such that no active rotation
752 of phagosomes was detected in cells that were treated with microtubule-disrupting drug nocodazole.
753
754 **(g) Determination of location of cell entry**
755 The boundary of the cell was manually traced in ImageJ according to the fluorescence emission
756 (ex/em 561/586 nm) of the cell in Ringer's solution containing trypan blue (Supplementary Fig.
757 27a). The boundary and the center of the nucleus was manually traced in ImageJ based on the bright
758 field image of the given cell [48, 69] (Supplementary Fig. 27b).
759
760 **(h) Calculation of Mean-Square Displacements (MSD)**
761 Time-resolved MSD shown in Fig. 4d was analyzed using custom MATLAB algorithms. Briefly,
762 the MSD values of each single phagosome trajectories were calculated as a function of lag time $\boldsymbol{\delta t}$
763 based on the following equation:
764 $$\mathrm{MSD}(\delta t) = < \Delta R(t)^2 > = < (R(t+\delta t) - R(t))^2 > \quad (5)$$
765 Where $(R(t + \delta t) - R(t))$ is end-to-end displacement of an individual particle from the time point t
766 to $t + \delta t$.

767

768 **Transmission Electron Microscopy**

769 Cell samples for TEM imaging were prepared based on a previously reported protocol with slight
770 modification [66]. Particle sensors were incubated with cells for 50 min at 37 °C before trypsinization.
771 After centrifugation, the cell pellet was fixed on ice for 1 h by using a mixture of 2.5% (w/v)
772 glutaraldehyde and 1% (w/v) osmium tetroxide in 1×PBS buffer. Subsequently, the pellet was
773 stained in 0.5% (w/v) uranyl acetate aqueous solution for 12 h on ice. Cell pellets were dehydrated
774 sequentially in a series of ice-cold aqueous solutions containing 30% (v/v), 50%, 75%, 90%, 95%
775 and 100% ethanol for 5 min each. Dehydration in 100% (v/v) ethanol was repeated three times at
776 room temperature. The dehydrated cell pellet was immersed sequentially in resin infiltration
777 solutions that contain ethanol and Spurr's resin at various volume ratio (ethanol: resin, 2:1, 1:1 and
778 1:2) for 30 min each at room temperature. Cells were cured in 100% resin for 18 h at 65°C prior to
779 microtome sectioning. Sections were stained with 2% (w/v) uranyl acetate for 10 min before
780 imaging. Samples were imaged with a JEOL JEM-1010 Transmission Electron Microscope
781 (Electron Microscopy Center, Indiana University).

782

783 **References**


784 1. Harrison RE, Grinstein S. Phagocytosis and the microtubule cytoskeleton. *Biochem Cell*
785 *Biol* **80**, 509-515 (2002).
786
787 2. Al-Haddad AH*, et al.* Myosin va bound to phagosomes binds to F-actin and delays
788 microtubule-dependent motility. *Mol Biol Cell* **12**, 2742-2755 (2001).
789
790 3. Araki N. Role of microtubules and myosins in Fc gamma receptor-mediated phagocytosis.
791 *Front Biosci* **11**, 1479-1490 (2006).
792
793 4. Kelleher JF, Titus MA. Intracellular motility: How can we all work together? *Curr Biol* **8**,
794 R394-R397 (1998).
795
796 5. Oberhofer A*, et al.* Molecular underpinnings of cytoskeletal cross-talk. *P Natl Acad Sci*
797 *USA* **117**, 3944-3952 (2020).
798

6. Steinberg B, Huynh K, Grinstein S. Phagosomal acidification: measurement, manipulation and functional consequences.). Portland Press Ltd. (2007).

7. Lennon-Duménil A-M*, et al.* Analysis of protease activity in live antigen-presenting cells shows regulation of the phagosomal proteolytic contents during dendritic cell activation. *J Exp Med* **196**, 529-540 (2002).

8. Rybicka JM, Balce DR, Chaudhuri S, Allan ERO, Yates RM. Phagosomal proteolysis in dendritic cells is modulated by NADPH oxidase in a pH-independent manner. *Embo J* **31**, 932-944 (2012).

9. Smith LM, May RC. Mechanisms of microbial escape from phagocyte killing. *Biochem Soc Trans* **41**, 475-490 (2013).

10. Cossart P, Helenius A. Endocytosis of viruses and bacteria. *Cold Spring Harb Perspect Biol* **6**, (2014).

11. Kagan JC, Roy CR. Legionella phagosomes intercept vesicular traffic from endoplasmic reticulum exit sites. *Nat Cell Biol* **4**, 945-954 (2002).

12. Blocker A, Griffiths G, Olivo JC, Hyman AA, Severin FF. A role for microtubule dynamics in phagosome movement. *Journal of Cell Science* **111**, 303-312 (1998).

13. Keller S, Berghoff K, Kress H. Phagosomal transport depends strongly on phagosome size. *Sci Rep* **7**, 17068 (2017).

14. Jiang M*, et al.* Microtubule motors transport phagosomes in the RPE, and lack of KLC1 leads to AMD-like pathogenesis. *Journal of Cell Biology* **210**, 595-611 (2015).

15. Rybicka JM, Balce DR, Khan MF, Krohn RM, Yates RM. NADPH oxidase activity controls phagosomal proteolysis in macrophages through modulation of the lumenal redox environment of phagosomes. *Proc Natl Acad Sci U S A* **107**, 10496-10501 (2010).

16. Guerin I, de Chastellier C. Disruption of the actin filament network affects delivery of endocytic contents marker to phagosomes with early endosome characteristics: The case of phagosomes with pathogenic mycobacteria. *Eur J Cell Biol* **79**, 735-749 (2000).

17. Gibbs D, Kitamoto J, Williams DS. Abnormal phagocytosis by retinal pigmented epithelium that lacks myosin Vila, the Usher syndrome 1B protein. *P Natl Acad Sci USA* **100**, 6481-6486 (2003).

18. Arora PD, Manolson MF, Downey GP, Sodek J, McCulloch CA. A novel model system for characterization of phagosomal maturation, acidification, and intracellular collagen degradation in fibroblasts. *J Biol Chem* **275**, 35432-35441 (2000).

19. Funato K, Beron W, Yang CZ, Mukhopadhyay A, Stahl PD. Reconstitution of phagosome-lysosome fusion in streptolysin O-permeabilized cells. *Journal of Biological Chemistry* **272**, 16147-16151 (1997).

20. Blocker A, Severin FF, Habermann A, Hyman AA, Griffiths G, Burkhardt JK. Microtubule-associated protein-dependent binding of phagosomes to microtubules. *J Biol Chem* **271**, 3803-3811 (1996).

21. Desjardins M, Huber LA, Parton RG, Griffiths G. Biogenesis of Phagolysosomes Proceeds through a Sequential Series of Interactions with the Endocytic Apparatus. *Journal of Cell Biology* **124**, 677-688 (1994).

22. Claus V*, et al.* Lysosomal enzyme trafficking between phagosomes, endosomes, and lysosomes in J774 macrophages enrichment of cathepsin H in early endosomes. *J Biol Chem* **273**, 9842-9851 (1998).

23. Savina A*, et al.* NOX2 controls phagosomal pH to regulate antigen processing during crosspresentation by dendritic cells. *Cell* **126**, 205-218 (2006).

24. Yu YQ, Gao Y, Yu Y. "Waltz" of Cell Membrane-Coated Nanoparticles on Lipid Bilayers: Tracking Single Particle Rotation in Ligand-Receptor Binding. *Acs Nano* **12**, 11871-11880 (2018).

25. Deriy LV*, et al.* Disease-causing Mutations in the Cystic Fibrosis Transmembrane Conductance Regulator Determine the Functional Responses of Alveolar Macrophages. *Journal of Biological Chemistry* **284**, 35926-35938 (2009).

26. Naufer A*, et al.* pH of endophagosomes controls association of their membranes with Vps34 and PtdIns(3)P levels. *Journal of Cell Biology* **217**, 329-346 (2018).

27. Nunes P, Guido D, Demaurex N. Measuring Phagosome pH by Ratiometric Fluorescence Microscopy. *Jove-J Vis Exp*, (2015).

28. Canton J, Khezri R, Glogauer M, Grinstein S. Contrasting phagosome pH regulation and maturation in human M1 and M2 macrophages. *Mol Biol Cell* **25**, 3330-3341 (2014).

29. Ogawa M, Kosaka N, Regino CAS, Mitsunaga M, Choyke PL, Kobayashi H. High sensitivity detection of cancer in vivo using a dual-controlled activation fluorescent imaging probe based on H-dimer formation and pH activation. *Mol Biosyst* **6**, 888-893 (2010).

30. Yates RM, Hermetter A, Russell DG. The kinetics of phagosome maturation as a function of phagosome/lysosome fusion and acquisition of hydrolytic activity. *Traffic* **6**, 413-420 (2005).

31. Gao Y, Anthony SM, Yu YQ, Yi Y, Yu Y. Cargos Rotate at Microtubule Intersections during Intracellular Trafficking. *Biophys J* **114**, 2900-2909 (2018).

32. Chen KJ, Wang B, Guan J, Granick S. Diagnosing Heterogeneous Dynamics in Single-Molecule/Particle Trajectories with Multiscale Wavelets. *Acs Nano* **7**, 8634-8644 (2013).

33. Sun-Wada GH, Tabata H, Kawamura N, Aoyama M, Wada Y. Direct recruitment of H+-ATPase from lysosomes for phagosomal acidification. *J Cell Sci* **122**, 2504-2513 (2009).

898 34. Pauwels AM, Trost M, Beyaert R, Hoffmann E. Patterns, Receptors, and Signals:
899 Regulation of Phagosome Maturation. *Trends Immunol* **38**, 407-422 (2017).
900
901 35. Riazanski V*, et al.* TRPC6 channel translocation into phagosomal membrane augments
902 phagosomal function. *P Natl Acad Sci USA* **112**, E6486-E6495 (2015).
903
904 36. Mcneil PL, Tanasugarn L, Meigs JB, Taylor DL. Acidification of Phagosomes Is Initiated
905 before Lysosomal-Enzyme Activity Is Detected. *Journal of Cell Biology* **97**, 692-702
906 (1983).
907
908 37. Duvvuri M, Krise JP. A novel assay reveals that weakly basic model compounds
909 concentrate in lysosomes to an extent greater than pH-partitioning theory would predict.
910 *Mol Pharmaceut* **2**, 440-448 (2005).
911
912 38. Fahrer J, Funk J, Lillich M, Barth H. Internalization of biotinylated compounds into
913 cancer cells is promoted by a molecular Trojan horse based upon core streptavidin and
914 clostridial C2 toxin. *N-S Arch Pharmacol* **383**, 263-273 (2011).
915
916 39. Horn MA, Heinstein PF, Low PS. Characterization of Parameters Influencing Receptor-
917 Mediated Endocytosis in Cultured Soybean Cells. *Plant Physiol* **98**, 673-679 (1992).
918
919 40. Pu J, Guardia CM, Keren-Kaplan T, Bonifacino JS. Mechanisms and functions of
920 lysosome positioning. *J Cell Sci* **129**, 4329-4339 (2016).
921
922 41. Jiang C, Lionberger TA, Wiener DM, Meyhofer E. Electromagnetic tweezers with
923 independent force and torque control. *Rev Sci Instrum* **87**, 084304 (2016).
924
925 42. Scott CC*, et al.* Phosphatidylinositol-4,5-bisphosphate hydrolysis directs actin remodeling
926 during phagocytosis. *Journal of Cell Biology* **169**, 139-149 (2005).
927
928 43. Huang NN*, et al.* Canonical and Noncanonical G-Protein Signaling Helps Coordinate
929 Actin Dynamics To Promote Macrophage Phagocytosis of Zymosan. *Mol Cell Biol* **34**,
930 4186-4199 (2014).
931
932 44. Hendricks AG, Holzbaur EL, Goldman YE. Force measurements on cargoes in living cells
933 reveal collective dynamics of microtubule motors. *Proc Natl Acad Sci U S A* **109**, 18447-
934 18452 (2012).
935
936 45. Kaufmann AM, Goldman SD, Krise JP. A fluorescence resonance energy transfer-based
937 approach for investigating late endosome-lysosome retrograde fusion events. *Anal*
938 *Biochem* **386**, 91-97 (2009).
939
940 46. Yates RM, Russell DG. Phagosome maturation proceeds independently of stimulation of
941 toll-like receptors 2 and 4. *Immunity* **23**, 409-417 (2005).
942
943 47. Huynh KK, Eskelinen EL, Scott CC, Malevanets A, Saftig P, Grinstein S. LAMP proteins
944 are required for fusion of lysosomes with phagosomes. *EMBO J* **26**, 313-324 (2007).
945
946 48. Dumas A*, et al.* The HIV-1 protein Vpr impairs phagosome maturation by controlling
947 microtubule-dependent trafficking. *J Cell Biol* **211**, 359-372 (2015).

948
949 49. Blocker A, *et al.* Molecular requirements for bi-directional movement of phagosomes
950 along microtubules. *J Cell Biol* **137**, 113-129 (1997).
951
952 50. Rai A, Pathak D, Thakur S, Singh S, Dubey AK, Mallik R. Dynein Clusters into Lipid
953 Microdomains on Phagosomes to Drive Rapid Transport toward Lysosomes. *Cell* **164**,
954 722-734 (2016).
955
956 51. Rai AK, Rai A, Ramaiya AJ, Jha R, Mallik R. Molecular Adaptations Allow Dynein to
957 Generate Large Collective Forces inside Cells. *Cell* **152**, 172-182 (2013).
958
959 52. Ferro LS, Can S, Turner MA, ElShenawy MM, Yildiz A. Kinesin and dynein use distinct
960 mechanisms to bypass obstacles. *Elife* **8**, (2019).
961
962 53. Harrison RE, Bucci C, Vieira OV, Schroer TA, Grinstein S. Phagosomes fuse with late
963 endosomes and/or lysosomes by extension of membrane protrusions along microtubules:
964 role of Rab7 and RILP. *Mol Cell Biol* **23**, 6494-6506 (2003).
965
966 54. Gowrishankar S, *et al.* Massive accumulation of luminal protease-deficient axonal
967 lysosomes at Alzheimer's disease amyloid plaques. *P Natl Acad Sci USA* **112**, E3699-
968 E3708 (2015).
969
970 55. Johnson DE, Ostrowski P, Jaumouille V, Grinstein S. The position of lysosomes within
971 the cell determines their luminal pH. *Journal of Cell Biology* **212**, 677-692 (2016).
972
973 56. Balderhaar HJK, Ungermann C. CORVET and HOPS tethering complexes - coordinators
974 of endosome and lysosome fusion. *J Cell Sci* **126**, 1307-1316 (2013).
975
976 57. Kissing S, *et al.* Vacuolar ATPase in Phagosome-Lysosome Fusion. *Journal of Biological*
977 *Chemistry* **290**, 14166-14180 (2015).
978
979 58. Pelfrene A, Cave MR, Wragg J, Douay F. In Vitro Investigations of Human
980 Bioaccessibility from Reference Materials Using Simulated Lung Fluids. *Int J Environ*
981 *Res Public Health* **14**, (2017).
982
983 59. Zahn C, *et al.* Measurement of the magnetic moment of single Magnetospirillum
984 gryphiswaldense cells by magnetic tweezers. *Sci Rep* **7**, 3558 (2017).
985
986 60. Etoc F, Lisse D, Bellaiche Y, Piehler J, Coppey M, Dahan M. Subcellular control of Rac-
987 GTPase signalling by magnetogenetic manipulation inside living cells. *Nat Nanotechnol* **8**,
988 193-198 (2013).
989
990 61. FitzGerald LI, Johnston APR. It's what's on the inside that counts: Techniques for
991 investigating the uptake and recycling of nanoparticles and proteins in cells. *J Colloid*
992 *Interf Sci* **587**, 64-78 (2021).
993
994 62. Jeschke A, Haas A. Sequential actions of phosphatidylinositol phosphates regulate
995 phagosome-lysosome fusion. *Mol Biol Cell* **29**, 452-465 (2018).
996

63. Jeschke A, *et al.* Phosphatidylinositol 4-phosphate and phosphatidylinositol 3-phosphate regulate phagolysosome biogenesis. *P Natl Acad Sci USA* **112**, 4636-4641 (2015).

64. Becken U, Jeschke A, Veltman K, Haas A. Cell-free fusion of bacteria-containing phagosomes with endocytic compartments. *Proc Natl Acad Sci U S A* **107**, 20726-20731 (2010).

65. Micheva KD, O'Rourke N, Busse B, Smith SJ. Array tomography: semiautomated image alignment. *Cold Spring Harb Protoc* **2010**, pdb prot5527 (2010).

66. Sanchez L, Yi Y, Yu Y. Effect of partial PEGylation on particle uptake by macrophages. *Nanoscale* **9**, 288-297 (2017).

67. Le-Bury G, Deschamps C, Dumas A, Niedergang F. Phagosome Migration and Velocity Measured in Live Primary Human Macrophages Infected with HIV-1. *Jove-J Vis Exp*, (2016).

68. Gross SP, Tuma MC, Deacon SW, Serpinskaya AS, Reilein AR, Gelfand VI. Interactions and regulation of molecular motors in Xenopus melanophores. *Journal of Cell Biology* **156**, 855-865 (2002).

69. Ba QL, Raghavan G, Kiselyov K, Yang G. Whole-Cell Scale Dynamic Organization of Lysosomes Revealed by Spatial Statistical Analysis. *Cell Reports* **23**, 3591-3606 (2018).

**Acknowledgments:** We thank Prof. Sergio Grinstein at University of Toronto for his helpful discussion. We thank Mr. Andy Alexander at the Electronic Instrument Services of Indiana University for assistance with the setup of magnetic tweezers. We thank Dr. Barry Stein at the IUB Electron Microscopy Imaging Center, Dr. Jim Power at the IUB Light Microscopy Imaging Center (LMIC), Dr. Yi Yi at the Nanoscale Characterization Center for assistance with instrument use.

**Funding:** The development of single-particle rotational tracking method was supported by the National Science Foundation, Division of Chemical, Bioengineering, Environmental, and Transport Systems under Award No. 1554078. All other research reported in this publication was supported by the National Institute of General Medical Sciences of the NIH under Award No. R35GM124918 (Y. Y.). G.F.W.W. is supported by a Vanier Canada Graduate Scholarship (CIHR). The content is

solely the responsibility of the authors and does not necessarily represent the official views of the NIH.

**Author contributions:** Y.-q. Y., Z. Z., and Y. Y. designed research; Y.-q. Y. and Z. Z. performed research and analyzed data; G. F. W. W. contributed critical reagents; Y.-q. Y., Z. Z., and Y. Y. wrote the paper and G.F.W. W. provided critical discussion.

**Competing interests:** The authors declare that they have no competing interests.

**Data and materials availability:** All data needed to evaluate the conclusions in the paper are present in the paper and/or the Supplementary Materials. Additional data related to this paper may be requested from the authors.

## Figures

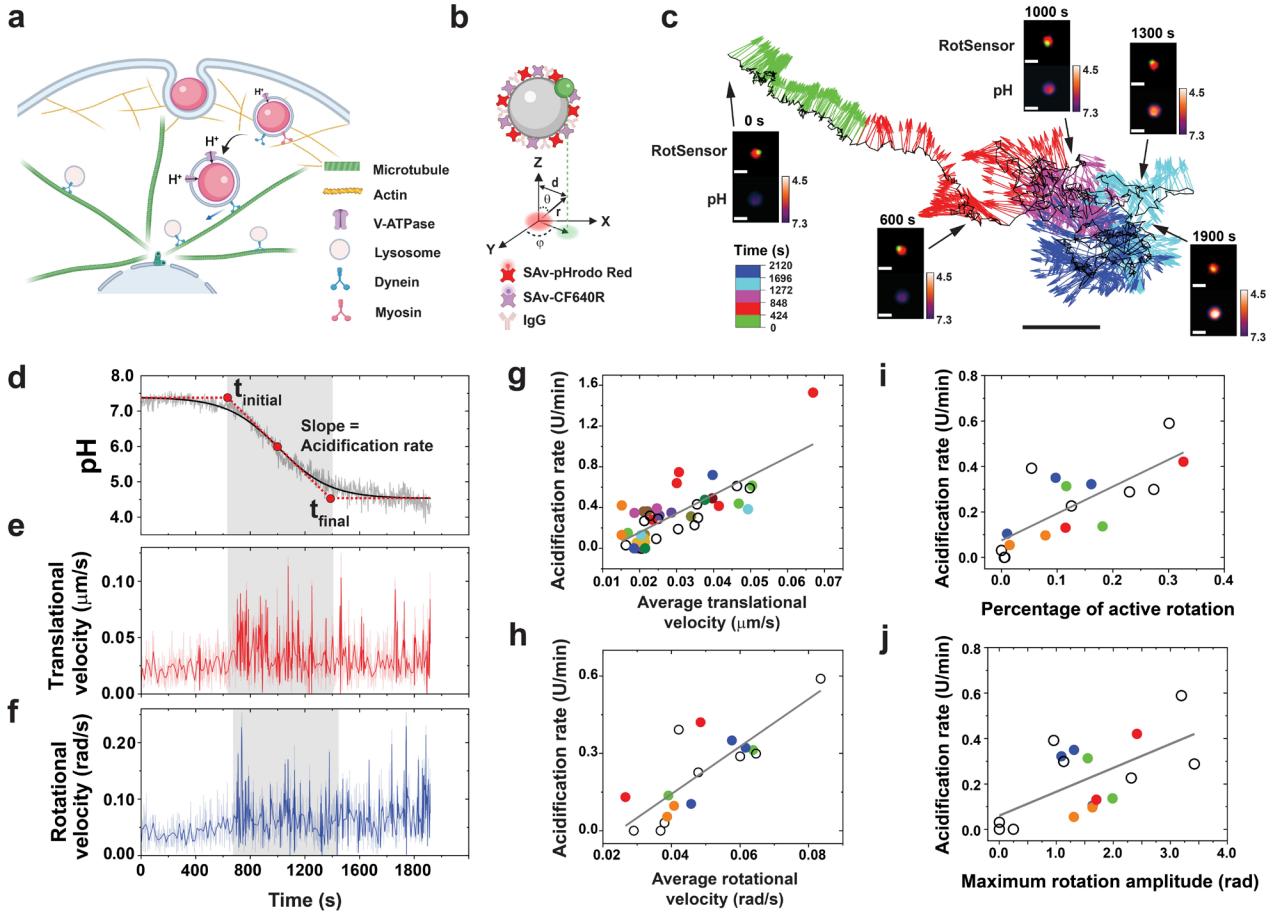


**Fig. 1 Simultaneous measurement of phagosome dynamics and acidification. a** Schematics showing internalization of pH-sensitive RotSensors into phagosomes in macrophage cells. **b** Schematic illustration of the RotSensor design. Each RotSensor contains a 1 μm silica particle tethered with a 100 nm yellow-green fluorescent particle. The silica particles were coated with streptavidin (SAv)-pHrodo Red (pH reporter) and SAv-CF640R (reference). The azimuthal (φ) and polar (θ) angles of each pH-RotSensor were analyzed based on its projection fluorescence image. d and r denote the projection inter-particle distance and the physical inter-particle distance, respectively. **c** A representative trajectory of a pH-RotSensor-containing phagosome. Vectors indicates the orientation of the pH-RotSensor and are color-coded based on time. Scale bar, 2 μm. Insets show fluorescence images of the RotSensor (top) and the pH response (bottom). Scale bar, 1 μm. **d-f** Line plots showing acidification (**d**), translational (**e**) and rotational velocities (**f**) of the pH-RotSensor-containing phagosome in **c**. The acidification profile is fitted with sigmoidal-Boltzmann function to determine the initial pH, final pH, the period of rapid acidification ($t_{initial}$ to $t_{final}$), and acidification rate. The period of rapid acidification is highlighted in grey. Darker lines in **e** and **f** are velocity values after wavelet denoising. **g** and **h** Scattered plots showing acidification rates against translational (**g**) and rotational velocities (**h**) of single phagosomes. Each data point represents one single phagosome. Data points from multiple phagosomes within the same cells are shown in the same solid color. Data points from cells containing only one phagosome are shown as black circles. N =

42 phagosomes from 24 cells for translational tracking, and 17 phagosomes from 12 cells for rotational tracking. Pearson's coefficients of 0.78 and 0.81 were obtained in **g** and **h**, respectively. **I** and **j** Scatter plots showing acidification rates against percentage of active rotation (**i**) and maximum rotation amplitude (**j**) of single phagosomes during rapid acidification period. N = 17 phagosomes from 12 cells. Pearson's coefficients of 0.76 and 0.61 are obtained in **i** and **j**.

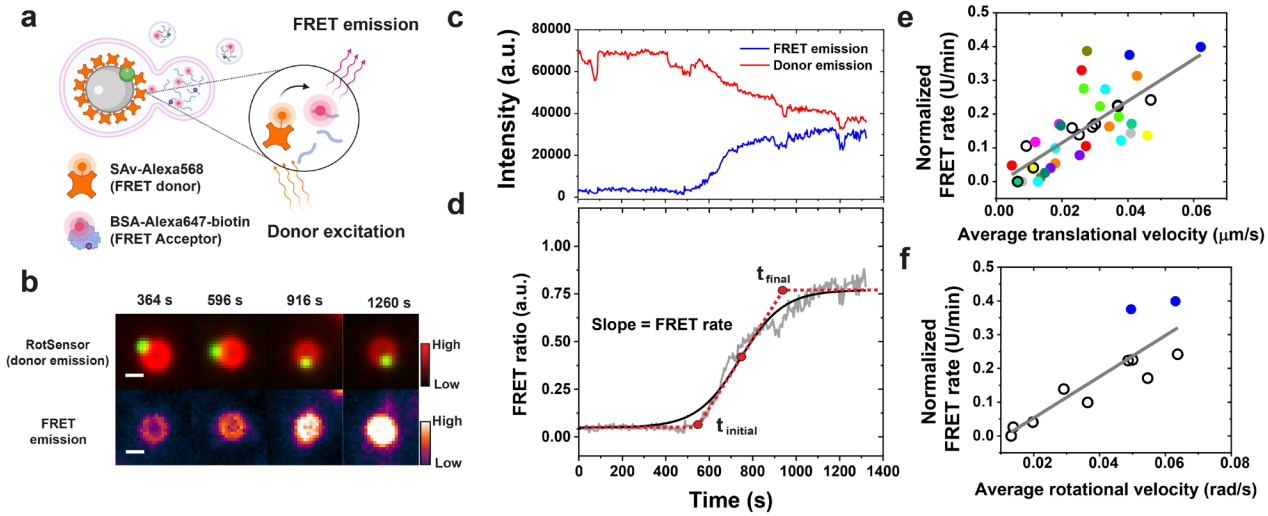


**Fig. 2 Simultaneous measurement of phagosome-lysosome fusion and phagosome transport dynamics. a** Schematic illustration of the Förster resonance energy transfer (FRET)-based phagosome-lysosome fusion assay. The FRET-RotSensor was coated with SAv-Alexa568 (FRET donor). BSA-Alexa647-biotin (FRET acceptor) was loaded into lysosomes. Phagosome fusion with lysosomes leads to intermixing between donor fluorophore (Alexa568) and fluid phase acceptor fluorophore (Alexa647) generating FRET emission (680 nm) under the donor excitation of 561 nm. **b** and **c** Fluorescence images and intensity plots showing the change of FRET emission (ex/em: 561/680 nm) and donor emission (red, ex/em: 561/586 nm) from a FRET-RotSensor (100 nm yellow-green nanoparticle in green) in a RAW264.7 macrophage. Scale bar, 2μm. **d** FRET ratio vs. time plot is fitted with sigmoidal-Boltzmann function (shown as the black solid line) to determine the initial time point of phagosome-lysosome fusion ($t_{initial}$), the time point where FRET-signal reaches a plateau ($t_{final}$), and the FRET rate, as indicated by the red dotted line. **e** and **f** Scatter plots showing normalized FRET rate against translational (**e**) and rotational velocities (**f**) of single phagosomes during the period of its fusion with lysosomes. Each data point represents data from a single phagosome. Data points from multiple phagosomes within the same cells are shown in the same solid color. Data points from cells containing only one phagosome are shown as black circles. For translational tracking, N = 40 phagosomes from 22 cells. For rotational tracking, N = 11 phagosomes from 10 cells. The black lines indicate linear regression with a Pearson's coefficient of 0.75 in **e** and of 0.86 in **f**.

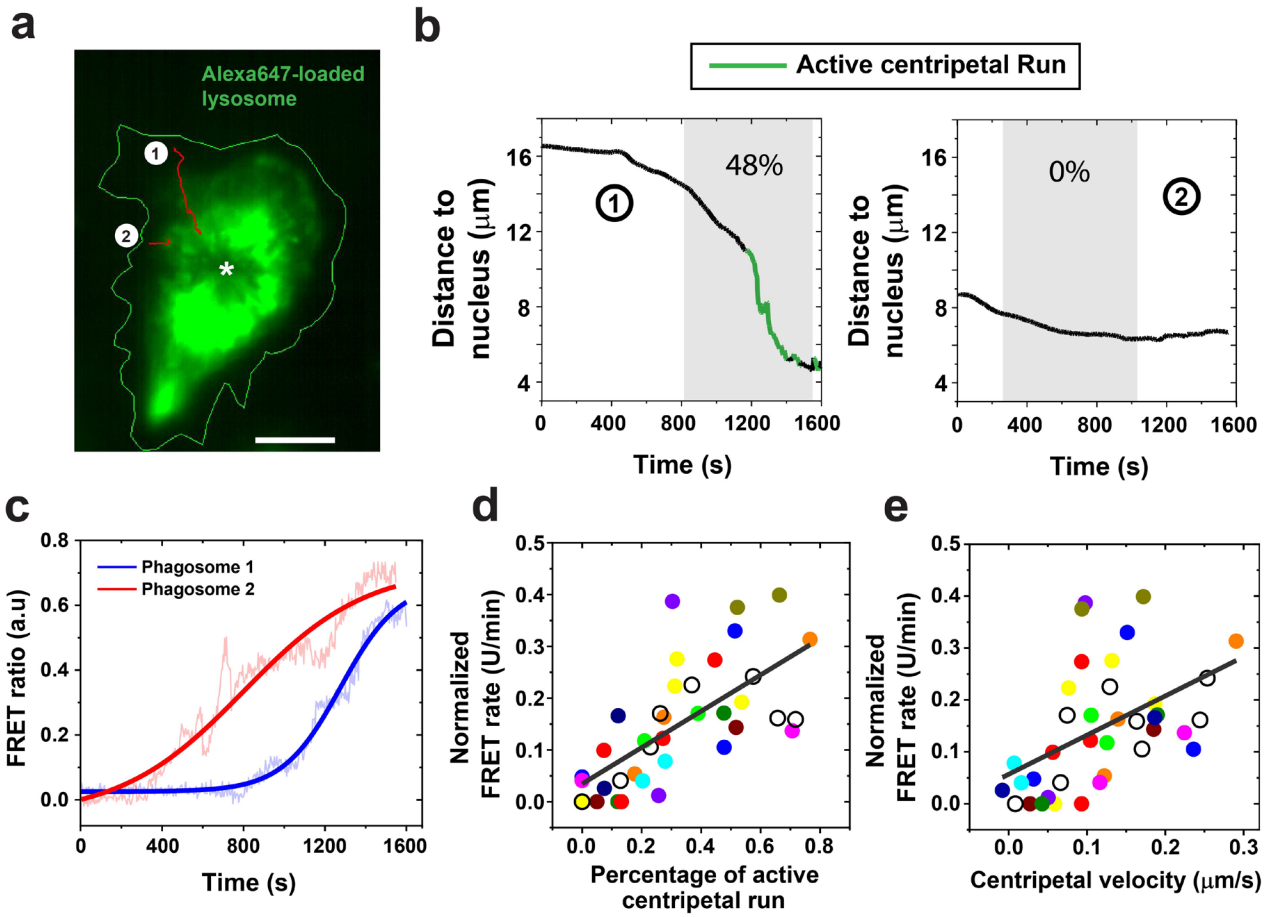


**Fig. 3 Correlation of phagosome-lysosome fusion kinetics with the centripetal motility of phagosomes. a** Fluorescence image showing a cell in which lysosomes were labeled with BSA-Alexa647-biotin. Green line indicates the cell periphery, and the asterisk indicates the centroid of the nucleus. The initial positions of two representative phagosomes were indicated by the two number-labeled white dots and their trajectories are shown in red. Scale bar, 10 μm. **b** Plots showing the phagosome-to-nucleus distance as a function of time for both the phagosomes indicated in **a**. Segments of active centripetal runs are highlighted in green. Grey shaded area indicates the effective transport distance of the phagosome from the time where it begins to fuse with lysosomes to the time when it reaches the nucleus boundary. The starting time of phagosome lysosome fusion was obtained based on sigmoidal fitting the FRET ratio vs. time plot. Phagosome #1 underwent active centripetal runs in 48% of the time during effective transport, whereas phagosome #2 had no active centripetal run. **c** FRET ratio vs. time plots for both phagosomes marked in **a**. Solid lines indicate sigmoidal-Boltzmann fitting to the data. **d** and **e** Scatter plots showing normalized FRET rate of single phagosomes plotted against the percentage of active centripetal motion (**d**) and centripetal velocity (**e**). Each data point represents data from a single phagosome. Data from multiple phagosomes inside the same cell are shown in the same solid color. Data from cells in which only one phagosome was studied are shown as black circles. N = 40 phagosomes

from 22 cells. The black lines indicate linear regression with a Pearson's coefficient of 0.68 and 0.49, respectively.

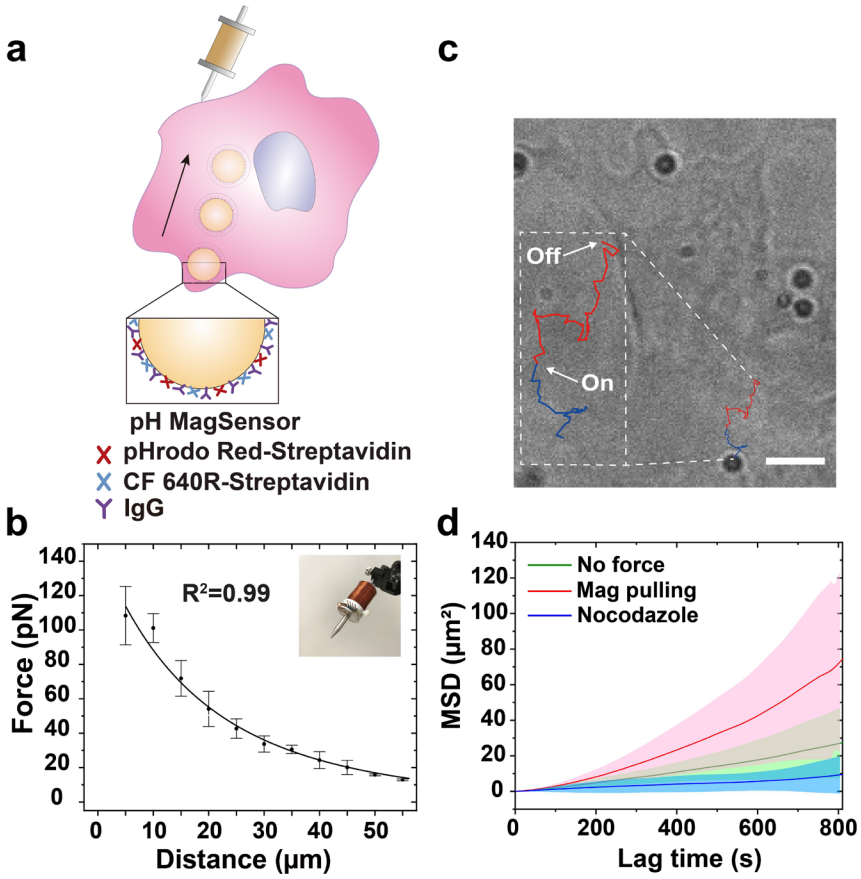


**Fig. 4 Phagosome degradation measurements during magnetically manipulated transport. a** Schematic illustration of the experimental setup. The magnetic gradient is generated by a homemade magnetic tweezers setup built on an inverted fluorescence microscope system. Magnetic pulling force was applied on MagSensors after their internalization into phagosomes. The 1 μm MagSensors were coated with SAv-pHrodo Red (pH indicator), SAv-CF640 (reference), and physically adsorbed IgG. **b** Calibration plot showing the magnetic force exerted on each MagSensor as a function of its distance to the tip of the magnetic tweezers solenoid (shown in inset). Error bars are standard deviations from 5 samples. **c** Bright-field image of a cell overlaid with the trajectory of a MagSensor-containing phagosome under magnetic pulling. The start and end time points of the exertion of magnetic force are indicated. The blue-colored segment of the trajectory indicates the movement of the MagSensor before cell entry; the red-colored segment of the trajectory indicates the intracellular movement of a MagSensor-containing phagosome under magnetic manipulation. Scale bar, 5 μm. **d** Mean-square displacements (MSD) calculated from trajectories of individual MagSensors under different conditions as indicated. Each line is an average of results from N = 10 phagosomes from 8 cells (no force), 9 cells (magnetic pulling), and 7 cells (nocodazole). Shaded areas indicate

standard deviations.

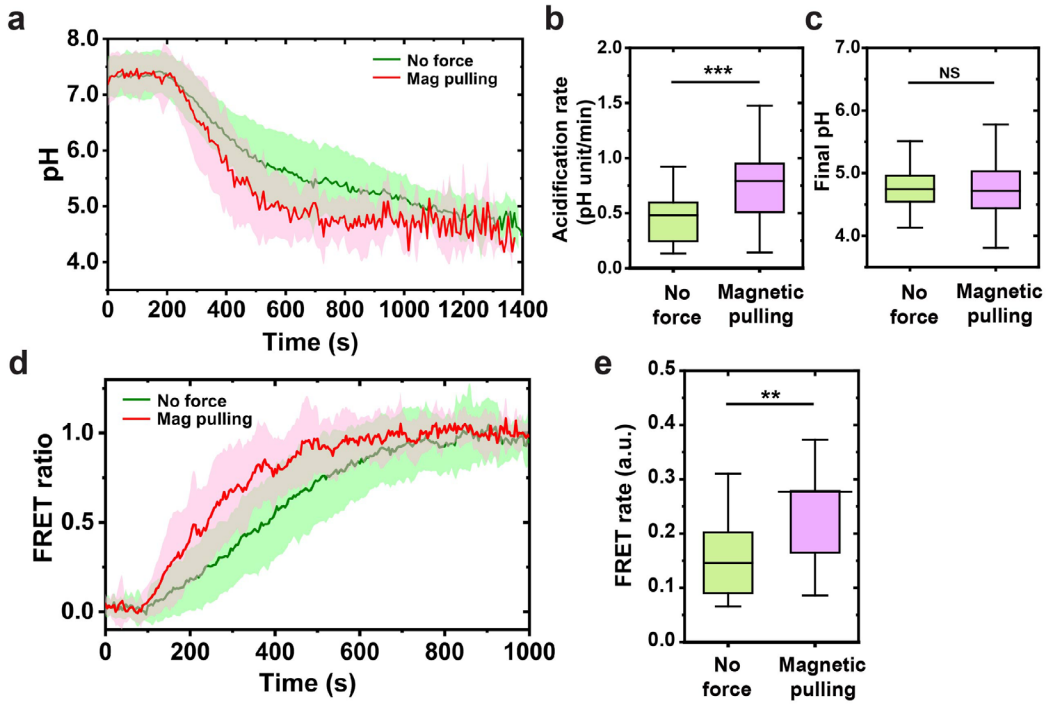


**Fig. 5 Phagosome acidification and phagosome-lysosome fusion under magnetic pulling. a** Line plots showing the average phagosome pH as a function of time with or without magnetic pulling as indicated. Each line plot is an average from 20 phagosomes. Shaded areas represent standard deviations. **b** Box graph showing the average acidification rate of phagosomes with or without magnetic pulling. The average acidification rate is 0.48 ± 0.34 pH unit/min without magnetic pulling (N = 33 phagosomes in 29 cells from 11 independent experiments) and 0.79 ± 0.54 pH unit/min with magnetic pulling (N = 38 phagosomes in 38 cells from 13 independent experiments). **c** Box graph showing the average final pH in different experiment conditions as indicated. The average final pH is 4.7 ± 0.3 without magnetic manipulation (N = 33) and 4.7 ± 0.4 with magnetic pulling (N = 38). **d** Line plots showing the average normalized FRET ratio as a function of time with or without magnetic pulling as indicated. The line curves are averaged from 20 individual phagosomes in each experimental condition. Shaded areas represent standard deviations. **e** Box graph showing the average normalized FRET rate in different experiment conditions as indicated. The average FRET rate is 0.15 ± 0.07 without magnetic manipulation (N = 20 phagosomes in 16 cells from 4 independent experiments) and 0.28 ± 0.21 with magnetic pulling (N = 20 phagosomes in 19 cells from 8 independent experiments). In **b**, **c** and **e**, each box plot indicates the mean (horizontal line) and the interquartile range from 25% to 75% of the corresponding data set. Statistical significance is highlighted by p-values (Mann-Whitney Test) as follows: ** $p < 0.01$, *** $p < 0.0001$, NS $p > 0.05$.